



저작자표시-비영리-변경금지 2.0 대한민국

이용자는 아래의 조건을 따르는 경우에 한하여 자유롭게

- 이 저작물을 복제, 배포, 전송, 전시, 공연 및 방송할 수 있습니다.

다음과 같은 조건을 따라야 합니다:



저작자표시. 귀하는 원저작자를 표시하여야 합니다.



비영리. 귀하는 이 저작물을 영리 목적으로 이용할 수 없습니다.



변경금지. 귀하는 이 저작물을 개작, 변형 또는 가공할 수 없습니다.

- 귀하는, 이 저작물의 재이용이나 배포의 경우, 이 저작물에 적용된 이용허락조건을 명확하게 나타내어야 합니다.
- 저작권자로부터 별도의 허가를 받으면 이러한 조건들은 적용되지 않습니다.

저작권법에 따른 이용자의 권리는 위의 내용에 의하여 영향을 받지 않습니다.

이것은 [이용허락규약\(Legal Code\)](#)을 이해하기 쉽게 요약한 것입니다.

[Disclaimer](#)

Master's Thesis

Fabrication and characterization of corrosion-
resistant surface layer on Mg-alloys by using large-
pulsed electron beam (LPEB) irradiation process

Woo Jin Lee

Department of Mechanical Engineering
Graduate school of UNIST

Fabrication and characterization of corrosion-
resistant surface layer on Mg-alloys by using large-
pulsed electron beam (LPEB) irradiation process

A thesis
submitted to the Graduate School of UNIST
in partial fulfillment of the
requirements for the degree of
Master of Science

Woo Jin Lee

06. 20. 2017 of submission

Approved by



Advisor

Prof. Hyung Wook Park

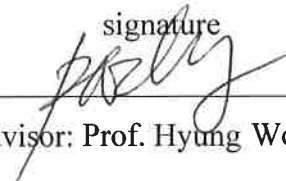
Fabrication and characterization of corrosion-resistant surface layer on Mg-alloys by using large-pulsed electron beam (LPEB) irradiation process

Woo Jin Lee

This certifies that the thesis of Woo Jin Lee is approved.


06. 20. 2017 of submission

signature



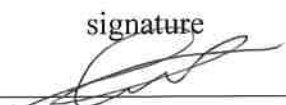
Advisor: Prof. Hyung Wook Park

signature



Prof. Young-Bin Park

signature



Prof. Namhun Kim

ABSTRACT

This research was begun for finding an appropriate industrial application of electron beam process. Particularly, since last decade, the surface treatment method using electron beam has been largely investigated. However, in the all published researches for Mg-alloys known for the world lightest-weight metal, the energy density level of the electron beam surface treatment was limited at only 2.5 - 3 J/cm² and the electrochemical performance has not yet been enhanced for engineering application. In this thesis, the energy density was increased up to 10 J/cm² with parameter optimization by applying large pulsed electron beam (LPEB) irradiation process on AZ31 plate specimens.

Firstly, through mathematical modelling of energy absorptivity of LPEB, the pitch of irradiation pattern was anticipated to adequate value. Applying the prediction model, the temperature profile was simulated by 2-D heat transfer equation. The estimated result was verified by real-time temperature measurement. The process was assessed how to be progressed rapid quenching and tempering. At over 20 cycles, the substrate temperature was above eutectic point (220°C) of Mg-Al alloy, but it was not increased over 300°C due to self-diffusion. To analyze the surface modification effects mechanically, it was demonstrated brightness, deformation of LPEB treated surface with the results of ball-on-disc wear test. The mechanical characteristics were enhanced by ~30% using LPEB process. For electrochemical analysis, the surface corrosion characteristics were qualitatively and quantitatively evaluated by 3-electrode cell test. Potentiodynamic polarization and electrochemical impedance spectroscopy was applied to evaluation. Then, low-field approximation and equivalent circuit modelling was used to certify the optimum LPEB parameter. At as-received sample, it presented irregular results since the oxide layer; it can protect the bare surface from corrosion, but it was easily damaged than the newly modified surface layer by LPEB process. The result was demonstrated that the electrochemical characteristics were improved by ~45%.

In addition, using the scanning electron microscopy (SEM) and energy dispersive spectroscopy (EDS) analyses, the morphology and the microstructure with chemical composition transformation were detailed discussed by metallurgically. As a result, it was presented that the tool mark was eliminated with new wavy surface morphology and the Al content was increased up to maximum level when the energy density is 5 J/cm². Consequently, the LPEB irradiation was verified that it can efficiently fabricate nano-grained corrosion-resistant surface layer with activating surface alloying induced by vaporization and re-melting process in Mg-Al binary alloy system. However, the technology was analyzed to require more development because surface defects were appeared by LPEB process due to inhomogeneous evaporation of Mg such as crater, crack, and micro-pole.

CONTENTS

ABSTRACTS.....	iv
CONTENTS.....	vi
LIST OF FIGURES.....	vii
LIST OF TABLES.....	x
NOMENCLATURE.....	xi
I . Introduction.....	1
1.1 Background.....	1
1.2 Research Objectives.....	4
1.3 Dissertation organization.....	6
II . Literature review.....	7
2.1 Surface treatment of Mg-alloy.....	7
2.2. Electron beam surface treatment.....	14
2.2.1. Large-pulsed electron beam process.....	14
2.2.2. Surface modification by electron beam irradiation.....	17
2.3. Summary.....	21
III. Surface modification of Mg-alloys using a large pulsed electron beam irradiation.....	22
3.1 Simulation of a large-pulsed electron beam irradiation.....	22
3.2. Experimental setup.....	29
3.2.1. Material.....	29

3.2.2. Surface treatment	29
3.2.3. Other equipment	31
3.3. Results and discussion	35
3.3.1. Temperature profile analysis	35
3.3.2. Mechanical characteristics analysis	36
3.3.3. Electrochemical characteristics analysis	44
3.4. Summary	48
IV. Metallurgical investigations on the surface of large pulsed electron beam treated Mg-alloys	50
4.1. Introduction	50
4.2. Microstructure transformation	53
4.3. Chemical composition transformation	56
4.4. Summary	59
V. Conclusions and recommendations	60
5.1. Conclusions	60
5.2. Recommendations	61
REFERENCES	62
ACKNOWLEDGEMENTS	67

LIST OF FIGURES

- Figure 1-1. (a) Mg production trend of 2002 - 2014 and (b) the projected market size with compound annual growth rate (CAGR) of non-ferrous metals in 2015 - 2020.
- Figure 1-2. Experimental process for parameter optimization of LPEB process on Mg-alloys.
- Figure 1-3. Flow chart of dissertation organization.
- Figure 2-1. Mechanism of corrosion reaction on the surface of Mg-alloys.
- Figure 2-2. (a) Comparison of material specific strength (Gupta et al.) and (b) Nyquist plot, (c) Bode magnitude plot, (d) Bode phase plot, and (e) XRD results of AZ31B, AM60, AMX602 and AZ91D specimens (Liao & Hotta).
- Figure 2-3. Conventional techniques of coating for Mg-alloys (Golabczak et al.).
- Figure 2-4. (a) Ion trajectories of 'SRIM2008 depth profile calculation' using 100 keV N⁺ ions, (b) Irradiated samples after 'Hardion⁺ technology treatments', (c) Schematic of LSM with EMS apparatus and (d) LSM with EMS treated specimen.
- Figure 2-5. Schematics of the different types of PEB machine; (a) Nadezhda, (b) GESA, and (c) PIKA.
- Figure 2-6. (a) Surface SEM morphologies of AZ31 Mg-alloy after HCPEB irradiation with different pulses, (b) Evolution of friction coefficients with friction time, and (c) Potentiodynamic polarization curves of AZ31 before and after HCPEB treatment (15 pulses).
- Figure 2-7. (a) HCPEB treated surface of AZ91, (b) EDS result of cross-section, (c) Microhardness modification through number of pulses, and (d) Polarization curve.
- Figure 2-8. Results comparison of (a) corrosion current density, (b) corrosion potential of steel, Ti-alloy, and Mg-alloy in potentiodynamic polarization analysis.
- Figure 3-1. Schematics of heat transfer mechanism when LPEB irradiation.
- Figure 3-2 (a) LPEB energy density at the center with accelerating voltage, (b) backscattering coefficient at different atomic number, (c) characteristic curve of energy density, and (d) electron beam energy absorptivity in magnesium with different accelerating voltage.
- Figure 3-3. (a) Gaussian distribution to the X-Y direction; the left graph is the experimental results and the right graph is the approximation result, (b) energy absorptivity of lateral direction, and (c) 3D energy absorption distribution of electron beam.
- Figure 3-4. (a) Thermal conductivity of AZ31, (b) Temperature profile of LPEB irradiation of AZ31, (c) the one pulse of LPEB process, and (d) the 400 pulses of LPEB process.
- Figure 3-5. (a) Graphics of PIKA Finish Machine, (b) Set-up of LPEB process, and (c) Schematics of LPEB surface treatment process.

Figure 3-6. Schematics of (a) the temperature monitoring system, (b) the ball-on-disc wear test system, and (c) the 3-electrode cell test system.

Figure 3-7. The equivalent circuit model of (a) bare surface and (b) LPEB treated surface.

Figure 3-8. Temperature profile at 1-, 5-mm depth of AZ31 sample during LPEB process.

Figure 3-9. Surface images of AZ31 samples at different number of cycles.

Figure 3-10. Surface images of (a) AM60 and (b) AZ91 at different accelerating voltage.

Figure 3-11. Deformation of AZ31 samples in height direction.

Figure 3-12. 1D surface roughness of AZ31 samples with different energy density.

Figure 3-13. 3D surface profile of AZ31 samples with the surface roughness.

Figure 3-14. COF profile of the Ball-on-disc wear test (a) ' $N = 10 \text{ N}$, $V = 260 \text{ mm/s}$ ($\omega = 500 \text{ rpm}$, $r_B = 5 \text{ mm}$)', (b) ' $N = 20 \text{ N}$, $V = 1 \text{ mm/s}$ ($\omega = 2 \text{ rpm}$, $r_B = 5 \text{ mm}$)', (c) ' $N = 20 \text{ N}$, $V = 105 \text{ mm/s}$ ($\omega = 200 \text{ rpm}$, $r_B = 5 \text{ mm}$)', and (d) maximum wear depth of the test (c).

Figure 3-15. 3D surface profile at wear scar of AZ31 samples in ' $N = 20 \text{ N}$, $V_d = 105 \text{ mm/s}$ '.

Figure 3-16. Evans-Hoar diagram of AZ31 samples: (a) 40 cycles, (b) 20 cycles.

Figure 3-17. (a), (b) Nyquist plot, (c), (d) Bode magnitude plot and (e), (f) Bode phase plot of AZ31

Figure 4-1. (a) Phase diagram of Mg-Al system and (b) schematics of LPEB surface modification onto Mg-alloys

Figure 4-2. The crystal structures of the two phases in the transformation system $\alpha\text{-Mg}/\beta\text{-Mg}_{17}\text{Al}_{12}$: (a) hcp $\alpha\text{-Mg}$, (b) bcc $\beta\text{-Mg}_{17}\text{Al}_{12}$ and (c) schematic diagram between hcp and bcc structures (Liu et al.).

Figure 4-3. SEM image of LPEB treated AZ31 and AM60 at different energy density.

Figure 4-4. SEM image of LPEB treated (a), (b) AZ31, (c), (d) AZ91 and (e) – (h) defects.

Figure 4-5. (a) Cross-section SEM image of LPEB treated AZ91 ($5 \text{ J/cm}^2 - 5 \text{ cycles}$), (b) the result of EDS line tracing of (a), and (c) - (h) Al/Mg content profiles of LPEB treated surface of Mg-alloys: (c) AZ31 at the energy density change, (d) AZ31 at the number of cycles change, (e) AM60 at the energy density change, (f) AM60 at the energy density change, (g) AZ91 at the energy density change, and (h) AZ91 at the number of cycles change.

Figure 4-6. EDS results of (a) as-received AZ31, (b) the AZ31 surface treated by the optimum LPEB process ($5 \text{ J/cm}^2 - 40 \text{ cycles}$), (c) the particle in the surface of AM60, and (d) the location.

LIST OF TABLES

Table 1-1. Comparison of surface treatment technology for Mg-alloys.

Table 2-1. Literature review on corrosion analysis of recent surface treatment method for Mg-alloys.

Table 2-2. Literature review of pulsed electron beam surface treatment on Mg-alloys.

Table 3-1. Material's chemical composition.

Table 3-2. LPEB process parameters.

Table 3-3. Corrosion analysis results obtained by linear polarization method.

Table 3-4. Fitting results of equivalent circuit modelling for EIS curve.

NOMENCLATURE

F	the Lorenz force
E	the electric field
B	the magnetic field
q	the charge of electron (-1.61×10^{-19} C)
v	the velocity of electron
m_e	the resting mass of the electron ($\sim 9.11 \times 10^{-31}$ kg)
γ	the relativistic factor ($1/(1 - v^2/c^2)^{1/2}$)
c	the speed of light ($\sim 3.00 \times 10^8$ m/s)
\hat{z}	the z direction vector
μ_0	the magnetic constant
n_t	the number of turns
I_s	the current of solenoid
I	the current of emitted electron
I^A	the Alfven's current
U_a	the accelerating voltage
V	the voltage
P	the power
E_{d0}	the energy density at the center
τ	the irradiation duration
S	the area of electron beam
r	the radius of electron beam
η	the efficiency
β	the backscattering coefficient
z_p	the maximum absorptivity depth
σ	the standard deviation
Z	the atomic number
r_0	the parameter of penetration
S_H	the heat source (W/m^3)
k	the thermal conductivity
ρ	the density
c_p	the specific heat (constant pressure)
H_F	the enthalpy of fusion

L_F	the latent heat of fusion
FP	the freezing point
MP	the melting point
T_0	the initial temperature
T_{\max}	the maximum temperature
ST	the service temperature
EP	the evaporation point
P_d	the power density (W/m^2)
h	the coefficient of convection
ε	the emissivity
σ_r	the Stefan-Boltzmann constant ($5.67 \times 10^{-8} [\text{W}/(\text{m}^2 \cdot \text{K}^4)]$)
T_∞	the ambient temperature
T_{surr}	the surrounding temperature
T_A	the temperature of material A
T_B	the temperature of material B
COE	the center of energy absorption distribution
β_0	the backscattering coefficient when the electron beam irradiation path is not inclined
θ	the angle of electron beam
\varnothing_{eff}	the effective diameter of electron beam
Fo	the Fourier number
v_{corr}	the corrosion penetration depth rate
R_p	the polarization resistance
β_a	the anodic Tafel slop
β_c	the cathodic Tafel slop
A_w	the atomic weight
z_k	the charge number of the metallic ion
F	the Faraday constant (96500 [C/mol])
i_{corr}	the corrosion current density
R_{ct}	the charge transfer resistance
R_s	the solution resistance
R_f	the film resistance
C_f	the double layer capacitance in the film
C_{dl}	the double layer capacitance of the total redox surface

Q	the charge phase element
ΔZ_{\max}	the maximum deformation
N	the normal force of indented ball
V_d	the velocity of disc
ω	the rotational speed of disc
r_B	the radius between ball to disc center
R_{corr}	the corrosion resistance

I . Introduction

1.1. Background

Today, by amazing developments of the advanced material engineering, the non-ferrous alloys are gradually highlighted for a substitute of the traditional structural materials. In the aviation and automobile industries, the steel (Fe-C-others) has been altered to the more innovative alloys based on aluminum (Al), titanium (Ti), magnesium (Mg) and the other non-ferrous metals (Ni, Co, Cr, Mo and etc.) . Referred to Figure 1-1, the Mg-alloys are going to be more and more fascinated among them. Generally, the reasons of the Mg-alloy's competitiveness are (i) high machinability and (ii) high functionality. For the machinability, 'mold and die-cast' and 'machining', known as the easy and low cost process, are regularly used for producing the final Mg-alloy's merchandise [1]. In the view of the functionality, the Mg-alloys are lighter than the Al-alloys by ~30%. Then, the biocompatibility of the Mg-alloys (Mg-Y-Nd-HRE) is also known as nobler to the Ti-alloys (Ti-6Al-4V, Ti-6Al-7Nb) in the some experimental cases applying for bio-implants [2]. From now on, the important issues of this thesis will be discussed; (i) surface treatment technologies for the Mg-alloys and (ii) methods to define the characteristics of Mg-alloys.

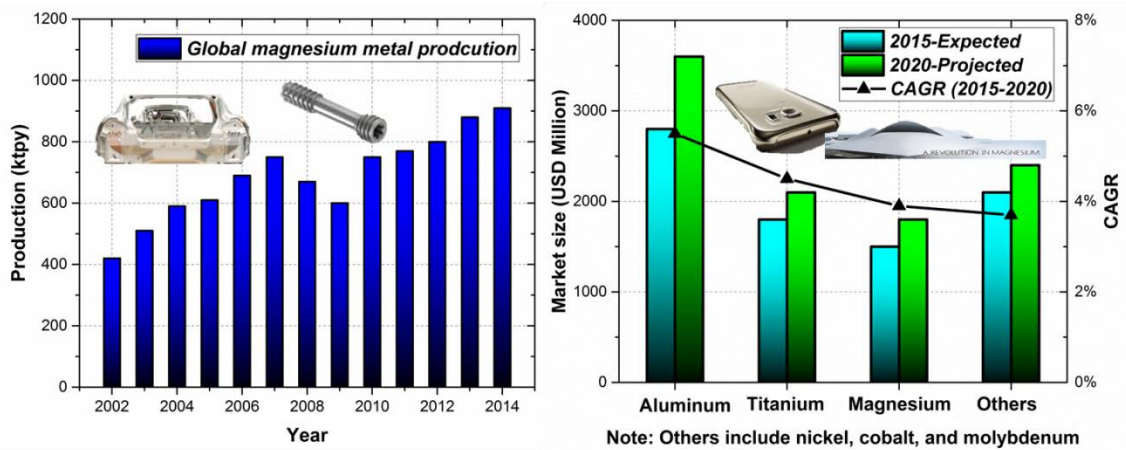


Figure 1-1. (a) Mg production trend of 2002 - 2014 [3] and (b) the projected market size with compound annual growth rate (CAGR) of non-ferrous metals in 2015 - 2020 [4].

First of all, the Mg is the world lightest-weight metal as the atomic number is 12, according to the periodic table. And then, because of a good moldability, the Mg-alloys are more recommended for the metal-based mass-production system than the newly developed composite materials such as fiber reinforced polymers (FRP) and nano-composites. Besides, its good damping and electromagnetic interference (EMI) shielding properties are also well acknowledged. However, for the reasons of the high chemical reactivity of the Mg in moisture with salty substances under marine environment and low friction durability in harsh scratched situation, it has not yet been widely utilized as a practical structural material.

Then, the various surface treatment technologies for the Mg-alloys have been studied for more advancement in surface quality and sterilization. The technology development process can be divided into two other classes according to the manufacturing view. The first is reducing an environmental pollution. Commonly, the pollution is generated during the chemical reaction process. And, the second is improvement of surface quality eliminating the surface defects such as delamination, micro-pore, crater, crack, and etc. The most critical defect of surface treatment is the delamination because the incomplete adhesion and heterogeneous bonding separates between the coated hard film and the soft substrate materials.

The surface treatment technologies for the Mg-alloys can be categorized to 10 divisions; 'grinding', 'polishing', 'buffing', 'dry-abrasive blasting', 'wet-abrasive blasting', 'barrel or bowl abrading', 'conversion coatings', 'organic coatings', 'cleaning', and 'plating'. Although simply the chemical polishing method can be used for enhancing the surface characteristics of the Mg-alloys in hand, the conversion coating method is actively studied for development of the standard film coating control systems such as electroplating, plasma electrolysis oxidation (PEO), and diamond-like carbon (DLC) coating. Until now, that research results show a many limitations, as you can check at the Table 1-1.

Electron beam (EB) is another prospective method can fulfil the environmental-friendly and less-defective surface modification as one of the directive energy beam irradiation (laser, ion) techniques. Particularly, for Mg-alloy enhancement, high-current pulsed-electron beam (HCPEB) process has been studied for the last decade [5-10]. Nevertheless, it needs more verification and advancement for optimizing the process parameters and corrosion characteristics of EB-treated Mg-alloys are still unsuitable for engineering application. Also, in the previous documents, the energy density level of HCPEB process is suggested only at the limited to 2.5 - 3 J/cm². Recently, according to Uno et al. [11] and Park et al. [12], large pulsed electron beam (LPEB) process shows distinct results compared to other EB processes, since it can cover the high energy density level up to maximum 10 J/cm² [13].

Table 1-1. Comparison of surface treatment technology for Mg-alloys.

Method	Principle	Performances	Limitations
Chemical polishing	Manual polishing using etchant	Surface roughness reduction	Manual process (cost)
Electroplating	Immersion in metallic solution	Bright color nodular structure, high adhesion, and cheap	Environmental pollution
Plasma electrolysis oxidation (PEO)	Anodizing with high electrical potential	Nano-film construction, high hardness/corrosion resistance	Hard controllability, delamination
Diamond-like carbon (DLC) coating	Sputtering and vacuum deposition	Environmental-friendly, high hardness/corrosion resistance	Long processing time, delamination
Ion implantation	Nitriding using ion beam	Environmental-friendly, dense microstructure surface	Long processing time, less quality
Laser surface modification	Focused laser beam irradiation	Environmental-friendly, self-quenching, and thick-film	Long processing time, harsh surface
Electron beam (EB) surface alloying	Pulsed electron beam irradiation	Low power consumption, reconstructed intermediate surface layer, fast	Crater, less quality

1.2. Research Objectives

The LPEB irradiation surface treatment for Mg-alloys is expected to several advantages; (i) high surface glossiness, (ii) high wear resistance, (iii) high corrosion resistance, and (iv) the possibility of mass-production. Although, there are various surface treatment methods of Mg-alloys, most of those methods are seen practically inefficient and cannot make better solution for the cost and defects. The LPEB treatment can overcome the previous problems by enhancing the surface quality without any other additional materials. Besides, the LPEB process enables to make fast and automatic finishing process. However, during the process of LPEB treatment, the working material is under vaporizing. Consider that the Mg-alloys are easily affected by heats and forces different from other heavy-metals, the most important issue is how to optimize the process parameters for appropriate LPEB treatment on Mg-alloys such as (i) irradiation pattern, (ii) energy density, and (iii) number of cycles.

To optimize the LPEB process, real-time monitoring and the performance examinations are needed. Firstly, for real-time monitoring, the temperature data of working material is investigated. Since the pulse duration is very short ($\sim 2 \mu\text{s}$), it is impossible to measure the perfect temperature profiles. Nonetheless, it can show generally the temperature changes whether the metal is well alloyed or not during the total shots of LPEB. Secondary, the process performances will be verified by the result parameters of the mechanical and electrochemical characteristics; (i) surface deformation (i) wear resistance, and (ii) corrosion resistance.

To determine whether the performance of the LPEB process is improved or degraded, the corrosion resistance properties are critically checked. Specifically, LPEB treatment can fabricate the stable and noble surface with eliminating the tool mark and reduce the surface defects known as weak to 'pitting corrosion'. Then, it is expected to eliminate the α - β boundary known to be weak to 'Galvanic corrosion' and construct dense grain microstructure with producing a nano-grained matrix and removing the slip planes related to dislocation and twinning. Also, for preventing the delamination, it needs well balanced brittleness and flexibility properties. LPEB treatment can increase the surface hardness with sustaining the toughness of original Mg-alloys. The most anticipated effect is chemical composition transformation. In Mg-alloying technologies, the Mg-alloys containing the high enriched Al content are stronger than the low Al content. However, it is known as very difficult to increase the Al content more than 9 wt.% because the solute-solution distribution characteristics. Different from the conventional methods, the LPEB treatment fabrication is expected to enable the special surface alloying by increasing Al content of the Mg-alloy surfaces. The reason is LPEB irradiation can vaporize the Mg selectively under the optimized energy conditions.

In this study, analysis has been demonstrated for evaluating the enhancements of the

mechanical and electrochemical properties of the Mg-Al alloys by the LPEB surface treatment. As a commonly commercialized Mg-Al alloy, AZ31 (Al 3%, Zn 1%) was assessed for the study because AZ31 has the most possibility for improvement of Al content among the other Mg-Al alloys (AZ91, AM60, and etc.). The energy density of LPEB was changed from 3 to 10 J/cm² and simultaneously the number of cycles also was changed from 1 to 100 for finding optimum process parameters. Then, verification tests were repeatedly conducted; ball-on-disc wear test as mechanical analysis and potentiodynamic polarization, electrochemical impedance spectroscopy (EIS) as electrochemical analysis. Lastly, scanning electron microscopy (SEM) and energy dispersive spectroscopy (EDS) analyses were applied for observation the microstructure and chemical composition transformations.

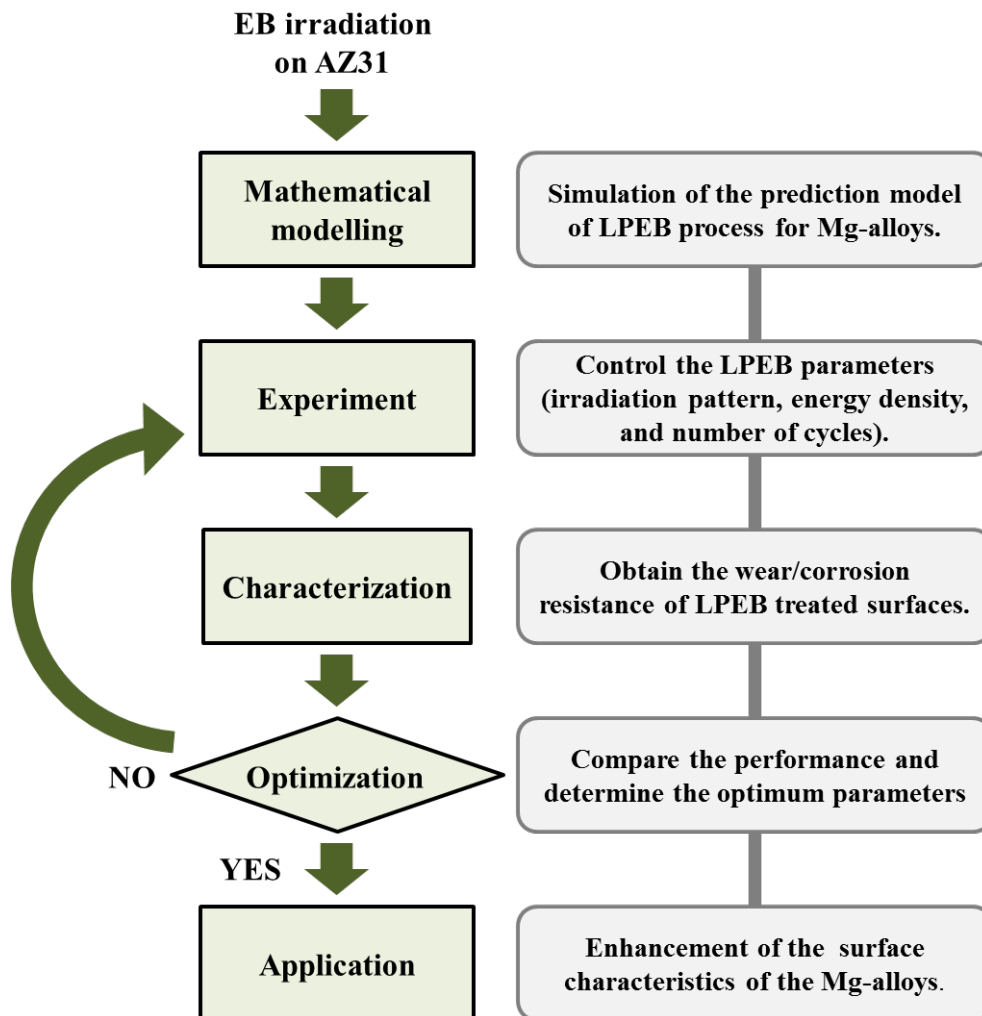


Figure 1-2. Experimental process for parameter optimization of LPEB process on Mg-alloys.

1.3. Dissertation organization

The introduction of this study is presented in Chapter 1. In Chapter 1, you can check the background knowledge of this thesis. Chapter 2 shows literature review. The literature review section is divided to the conventional surface treatment technologies for Mg-alloys and EB surface treatment. Then, Chapter 3 described the process optimization by introducing the experimental conditions and characterization results of the mechanical and electrochemical enhancements. Performances and limitations in the thesis of EB surface treatment for Mg-alloys are suggested in Chapter 3. The analysis of surface modification effects is comprised in Chapter 4. The metallurgical analysis is conducted for verification. Finally, Chapter 5 describes the conclusions and recommendations. This dissertation is laid out as follows in Figure 1-3.

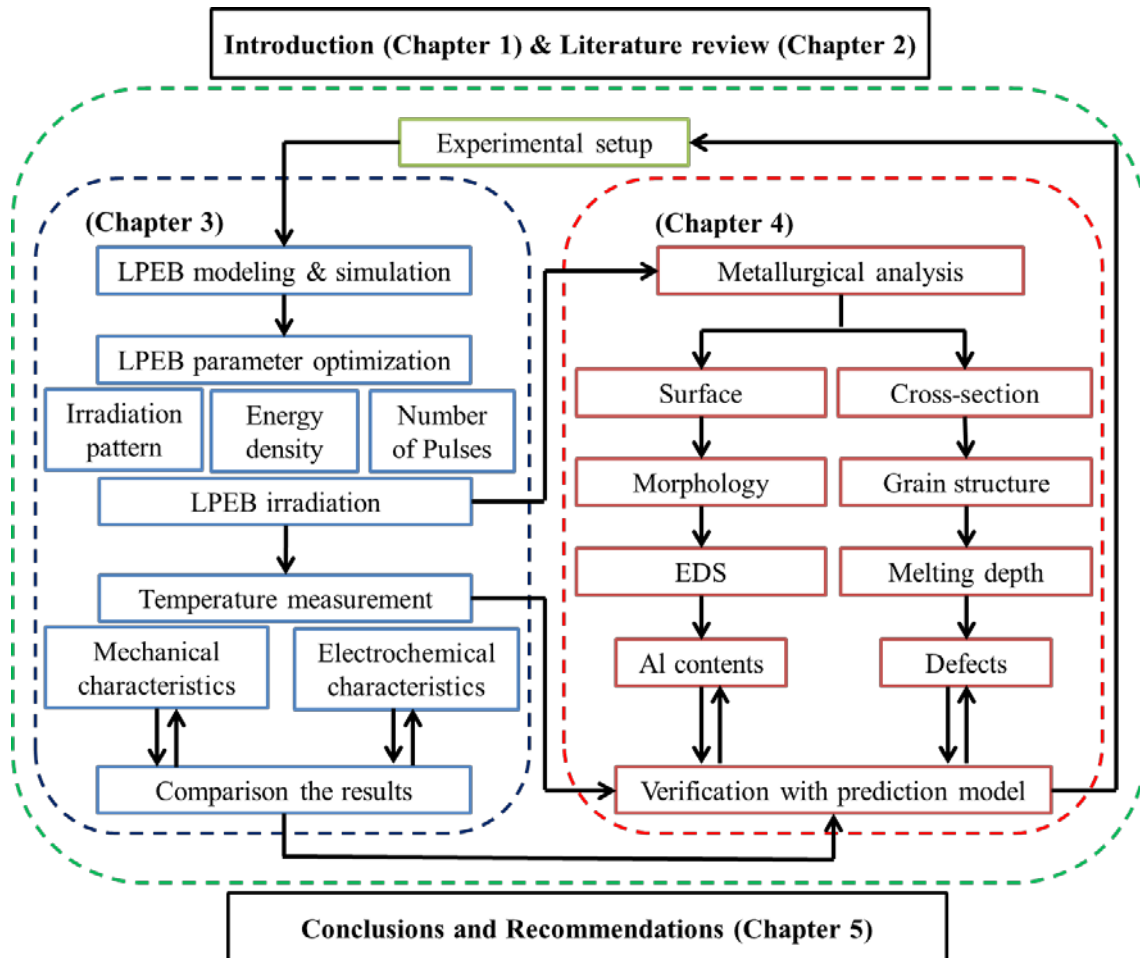


Figure 1-3. Flow chart of dissertation organization.

II. Literature review

This chapter presents the review of literature survey of the areas of studies. The literature review is divided into two groups; (i) surface treatment of Mg-alloy and (ii) EB surface treatment. The reviews on the LPEB process will include the results of the recent studies of electron beam surface treatment with various experimental parameters. The literature review of the characteristics of Mg-alloy will include the research on the electrochemical results of various surface treatments for the Mg-alloys.

2.1. Surface treatment of Mg-alloy

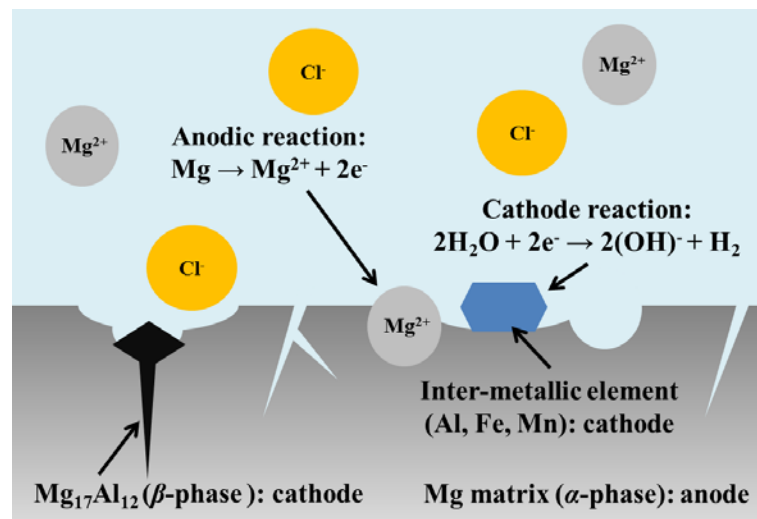
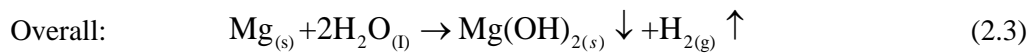
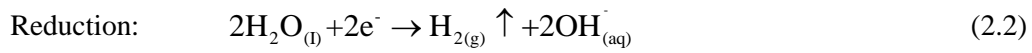


Figure 2-1. Mechanism of corrosion reaction on the surface of Mg-alloys.

Encouragingly, Chen et al. [14] showed the commercially-produced Mg (CP-Mg) plates have a self-organized oxide film by just remaining in atmosphere for a longtime. The oxide layer has been reported it can make well withstand the attacks from a corrosive environment. However, the oxide film is very thin (~ 1 μm) and fragile according to Avedesian et al. [15]. Therefore, it is very easily removed by mechanical impact in engineering applications. Figure 2-1 represents the corrosion reaction of Mg-alloys. If the chloride ion is existed in water solution, the ‘galvanic corrosion’ is mainly occurred at the α - β grain boundary (inter-metallic element), because Mg has high metal ionization tendency, the sequence is ordered such as ‘ $\text{Mg} > \text{Al} > \text{Zn} > \text{Fe} > \dots$ ’. Also, because of the ‘pitting corrosion’ generated owing to exterior incursions, which is occurred at the local defects and activates the corrosive products are spread laterally to the other unscratched zone [16]. So, it is very important to maintain the surface homogeneity and stability.

Referred to Yavov et al. [17], the Mg-alloys are known as hard to hand polishing due to generate hydrogen gas (H₂) easily explosive when the small Mg powders react with water (H₂O), the chemical reaction is described below:



For this reason, many researchers have been challenged to develop more successful protection methods for the CP-Mg plate. Hence, there are many tries to protect the CP-Mg plate from the harsh engineering environments in the academic area of ‘alloying’ and ‘surface treatment’.

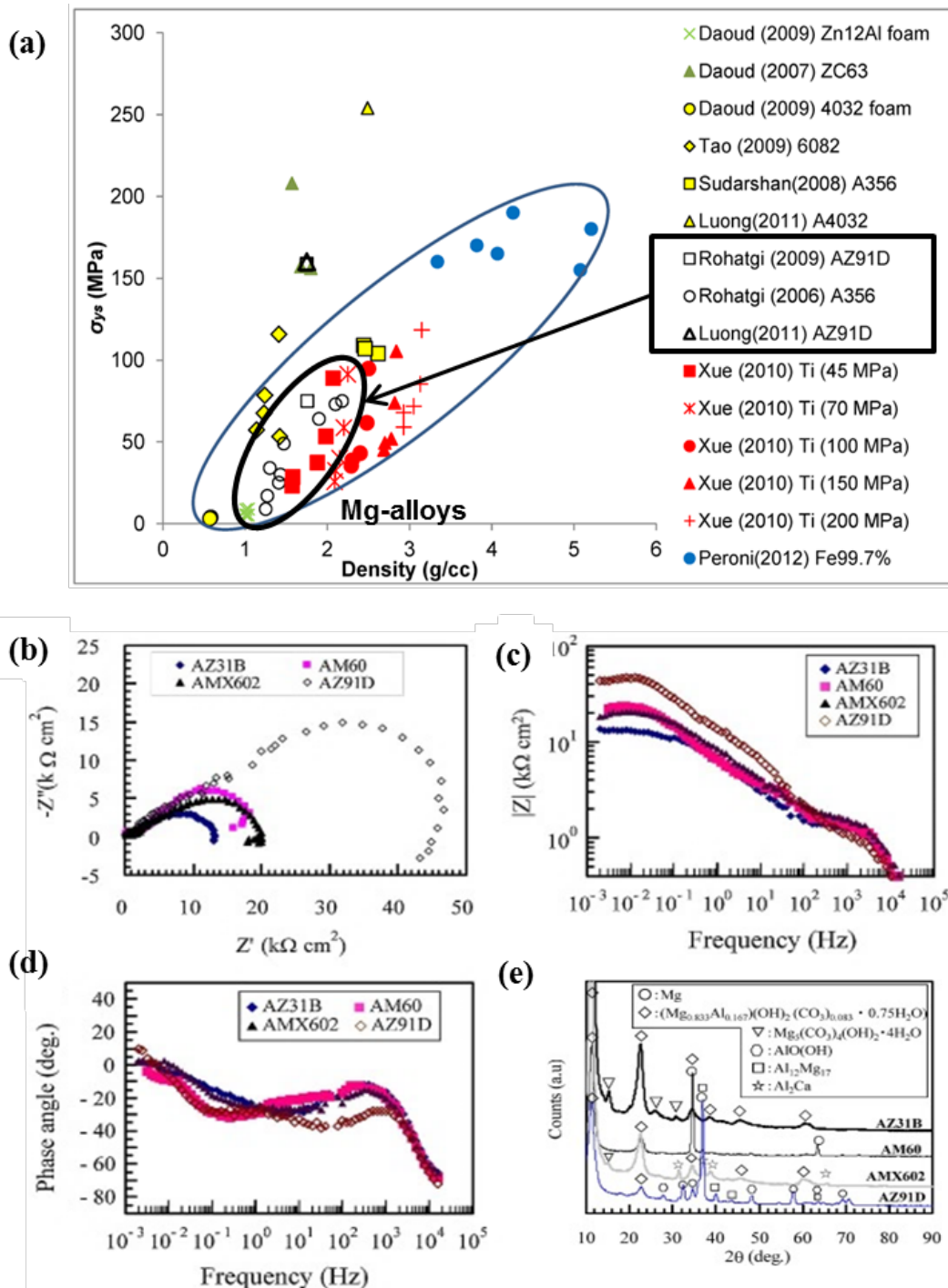


Figure 2-2. (a) Comparison of material specific strength (Gupta et al. [18]) and (b) Nyquist plot, (c) Bode magnitude plot, (d) Bode phase plot, and (e) XRD results of AZ31B, AM60, AMX602 and AZ91D specimens (Liao & Hotta [19]).

Ding et al. [20] has been asserted that the elemental Mg-alloying method is making appropriate multi-combination allotropic system with Al, zinc (Zn), manganese (Mn) and the rare-earth materials (Y, Nd, and etc.). From the last 30 years, this approach has been produced the commercialized Mg-alloys. Famous AZ, AM series and WE43 were provided by ‘Magnesium Elektron’. Figure 2-2 describes the mechanical performance of Mg-alloys and EIS diagram with XRD analysis results. The electrochemical impedance is ordered by Al content such that ‘AZ91D > AMX602 = AM60 > AZ31’. However, Mg-alloying with over enriched Al causes excessive brittleness. Hence, the maximum Al content is limited at ~9 wt.% in Mg-alloying process according to Pekguleryuz et al. [21]. Among them, the techniques of coatings manufacturing are ordered at Figure 2-3 divided to 6 categories. But, the assembling is less strict because the techniques are complicatedly overlapped each other. To the next topic, it is managed to the detail information of the coating technologies of Mg-alloys.

Techniques of coatings manufacturing of magnesium alloys					
(1) Electroplated coatings	(2) Conversion coatings	(3) Anodizing	(4) Gas-phase deposition	(5) Surface alloying	(6) Polymer coatings
Zinc immersion	Chromate	In fluoride bath	Ion implantation	Laser alloying	Painting coating
Nickel plating	Fluorozirconate	In alkaline bath	CVD	EB alloying	Sol-gel process
Alternative	Stannate	PEO	PVD		Powder coating
From noble metals	Phosphate-permanganate		Diffusion coating		Epoxidation
			Thermal spray deposition		Polymerization

Figure 2-3. Conventional techniques of coating for Mg-alloys (Golabczak et al. [22]).

Following the surface treatment technology development history, the ‘chemical vapor deposition (CVD)’ is eligible to be firstly discussed. Referred to Ponja et al. [23], the mechanism of CVD is generating chemical reaction for coating the other stable materials. Because the most CVD processes are performed in liquid, it is so called as a ‘wet method’. For example, there are numerous CVD methods for enhancing the Mg-alloys. The simplest CVD method is the ‘chemical polishing’ [24], which are accompanied with toxicant chemical solution. The chemical polishing is used for erasing the debris of the surface. And then, the ‘immersion method’ is using CVD conducted in ethanol solution bath mixed with nitric acid and acetic acid. After the adequate immersion time, the protected thin-layer can be formed. Also, the ‘porous-media deposition’ makes doping the nano oxide-film in sulfide acid solution using CVD. Among the well-known CVD methods, the ‘electroplating’ has been widely utilized for the conventional Mg-alloys surface treatment technology. Generally, it is using the copper pyrophosphate solution to protect the substrate materials. Especially, Dong et al. [25] introduced the ‘Chrome VI (Cr^{6+}) pickle electroplating’. It shows the performances; bright color, nodular structure, and high adhesion.

Recently, to avoid the toxicity to the human body and environmental pollution originating from the harmful chemical reagents, other alternatives have been actively reported. For instance, as the wet method, ‘anodizing’, ‘plasma electrolytic oxidization (PEO)’, ‘plasma spraying’, and ‘sol-gel’ techniques have been suggested. And as a ‘dry method’, ‘physical vapor deposition (PVD)’ and ‘direct energy beam irradiation method’ has been researched. The easiest way of the alternatives is anodizing. From Kwon et al. [26], the anodizing is using the mechanism of the ion transferring from the cathode to the anode materials in non-toxic solution. The PEO process is one of the anodizing methods. It is conducted with higher electrical potential than the basic anodizing process. Arrabal et al. [27] verified that performance of PEO; high corrosion resistance with less surface roughness. Since PEO can fabricate various functional coatings regardless of the target materials [28], it is anticipated to the best substitute for the conventional electroplating technologies.

On the other hand, the PVD technologies of the Mg-alloys have been developed in the only lab-scale applications at present. However, the PVD methods are expected to the future manufacturing solution because it can make freely control the coating parameters. The essential mechanism of PVD is ‘ion implantation’ which is by ‘sputtering effect’ and ‘vacuum deposition’ in vacuum. For example, the one of the most popular PVD surface treatments is diamond-like carbon (DLC, sp^3) and graphene (sp^2) coatings. Following Tański and Tomasz [29], in order to coating the nano carbon composite layer which is working by CVD process with the acetylene gas (C_2H_2) in vacuum chamber, the plasma-enhanced chemical vapor deposition (PECVD) method has been adapted. Also Ishizaki et al. [30] showed the fabrication of super hydrophobic film using PECVD.

Peng et al. [31] showed the ‘nitriding process’ of the pure Mg. the process is activated by negative electrical charging on the substrate under nitrogen (N_2) plasma. When N^+ ion is collided with substrate atoms, interstitial ion implantation is occurred and it causes cascaded dislocation in lattice structure. Also, referred to Figure 2-4 (a), Höche et al. [32] investigated ‘ion beam surface modification’ method for enhancing the surface of Mg-alloys. Eventually, the suggested PVD surface treatment technologies can increase the overall surface properties of the Mg-alloys similar to the coating materials. However, the delamination problem has been not yet completely solved as shown at Figure 2-4 (b).

Today, as one of directive energy beam irradiation methods, laser beam technology has been developed for surface alloying of the original surface of the Mg-alloys to reducing delamination problem. In Figure 2-4 (c), Zhou et al. [33] suggested ‘laser surface melting (LSM)’ with ‘electromagnetic stirrer (EMS)’ to improve the corrosion resistance of Mg-alloys remarkably by re-melting process with rapid self-quenching. It shows very thick (~1 mm) re-melting surface layer and deep heat affected zone (HAZ), but there are some plastic deformations with beam path due to the focused energy beam’s long duration as shown at Figure 2-4 (d). In Table 2-1, the current study trend of surface treatment for Mg-alloys is summarized in the view of corrosion analysis.

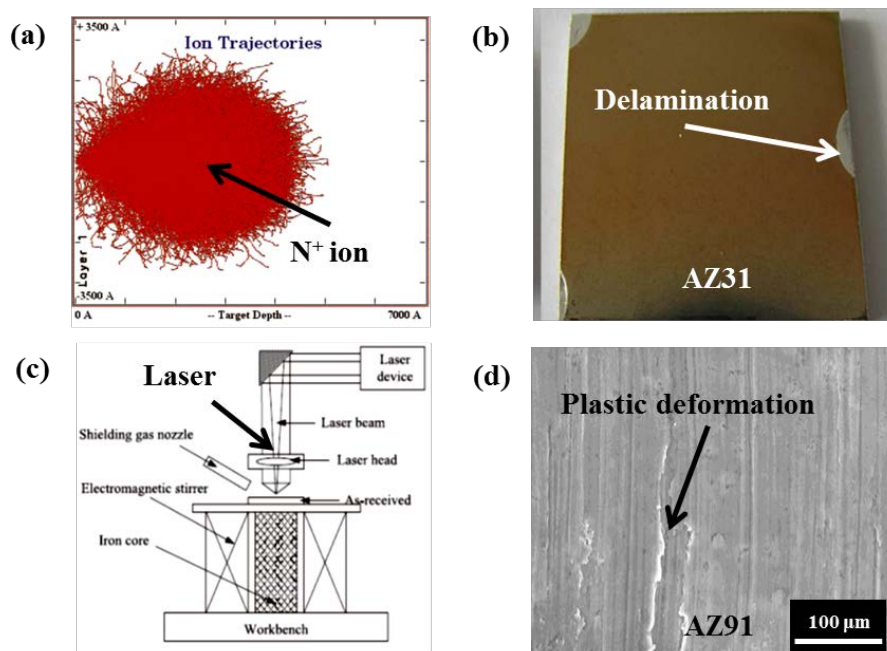


Figure 2-4. (a) Ion trajectories of ‘SRIM2008 depth profile calculation’ using 100 keV N^+ ions [32], (b) Irradiated samples after ‘Hardion⁺ technology treatments’ [32], (c) Schematic of LSM with EMS apparatus [33] and (d) LSM with EMS treated specimen [33].

Table 2-1. Literature review on corrosion analysis of recent surface treatment method for Mg-alloys

Anti-Corrosion Surface treatments : Authors (year)	Mat.	RE (CE)	Results (As-received -> Treated)
Laser (Ø 4 mm, 2 kW, 200 mm/m) : Majumdar et al. [34] (2003)	MEZ	SCE (Pt)	R_p : 15.07 mΩ·cm ² → 899.9 mΩ·cm ² i_{corr} : 69 mA/cm ² → 1.5 mA/cm ²
Heat treatment (T6) : Zhou et al. [33] (2010)	AZ91	SCE (Pt)	v_{corr} : 0.85 mm/y → 0.59 mm/y i_{corr} : 0.039 mA/cm ² → 0.027 mA/cm ²
Chemical conversion (PO ₄ ³⁻ /Mn, Ce) : Rocca et al. [35] (2010)	AZ91	SCE (Pt)	R_p : 1000 Ω·cm ² → 15000 Ω·cm ² i_{corr} : 0.35 mA/cm ² → 5 - 10 μA/cm ²
Ion implantation (65 keV N ⁺ ions) : Höche et al. [32] (2011)	AM50	Ag/AgCl (Pt)	R_p : 1512 Ω·cm ² → 2472 Ω·cm ²
HCPEB (3 J/cm ² , Ø 60 mm, 15 pulses) : Bo et al. [36] (2011)	AZ31	SCE (Pt)	i_{corr} : ~0.01 mA/cm ² at -1.51 V _{SCE} → ~0.000001 mA/cm ² at -1.36 V _{SCE}
Chemical conversion (C ₁₄ H ₂₈ O ₂ , FeCl ₃) : Zhao et al. [37] (2014)	AZ31	Ag/AgCl (Pt)	R_p : 200 Ω·cm ² → 1500 Ω·cm ² i_{corr} : 20.75 → 0.02579 μA/cm ²
HCPEB (3 J/cm ² , Ø 60 mm, 15 pulses) : Li et al. [6] (2014)	AZ91	SCE (Pt)	i_{corr} : 48 μA/cm ² at -1.59 V _{SCE}
Laser (600 W, 60 mm/s) : Taltavull et al. [38] (2014)	AZ91	Ag/AgCl (Graphite)	v_{corr} : 0.46 mm/y → 0.10 mm/y i_{corr} : 20.2 μA/cm ² → 7.3 μA/cm ²
PVD coating (MgAl + Al ₂ O ₃) : Smolik et al. [39] (2015)	AZ91	Ag/AgCl (Pt)	E_{corr} : -1.5 V _{SCE} → -1.18 V _{SCE}
HCPEB (3 J/cm ² , Ø 60 mm, 15 pulses) : Hao & Li [5] (2016)	AZ91	SCE (Pt)	i_{corr} : ~0.1 mA/cm ² at -1.55 V _{SCE} → ~0.001 mA/cm ² at -1.25 V _{SCE}
Laser (1500 W, Ø 3mm, 600 mm/m) : Zhou et al. [33] (2017)	AZ91	SCE (Pt)	i_{corr} : 0.3595 mA/cm ² → 0.06869 mA/cm ²

2.2. Electron beam surface treatment

2.2.1. Large pulsed electron beam process

The pulsed electron beam (PEB) is developed for magnifying the transferred heat generation power. Generally, the system of electron beam machine is divided to electron gun and vacuum chamber. And also, the electron gun consists of cathode filament, anode ring, solenoid lens, and high power supply unit. Simply describing the whole mechanism of the EB irradiation, firstly the electron is amplified by charging the cathode at emitter of the EB machine. It is enabled in plasma atmosphere. Using the anode ring charging in advance, the electron and the ion are steady dispersed. Theoretical modeling of electron beam is related to the electromagnetic laws. According to Mesyat [40], the theory of electron motion in vacuum has been studied in 1960 - 80s. Especially, it was documented that the LPEB is generated by ‘explosive electron emission (EEE)’ effect and it is accelerated by ‘explosive gap breakdown’ phenomenon and ‘Penning effect’.

The velocity of the emitted electrons is accelerated to one- or two-thirds of the speed of light induced a Lorenz force with electromagnetic fields. The force equilibrium of the electrons can be described as [40]:

$$F = q[E + (v \times B)] \quad (2.4)$$

$$m_e \gamma (dv / dt) = F - (qv / c^2)(v \cdot E) \quad (2.5)$$

$$B = \mu_0 n_t I_s \hat{z} \quad (2.6)$$

From Eq. (2.4), F is the Lorenz force, and E and B means the electric and magnetic fields, respectively. q is the charge of the electron (-1.61×10^{-19} C) and v is its velocity. Eq. (2.5) is expressed the relativistic equation of motion, written in Newton’s form. m_e is resting mass of the electron ($\sim 9.11 \times 10^{-31}$ kg), γ is the relativistic factor ($1/(1 - v^2/c^2)^{1/2}$), and c is the speed of light ($\sim 3.00 \times 10^8$ m/s). At Eq. (2.6), the magnetic field (B) is presented by constant form. It is directed to the emitter or the collector (\hat{z}) with the magnetic constant (μ_0) of the vacuum, and the number of turns (n_t), the current (I_s) of the solenoid coil. Applying the theory of relativity in homogeneous electromagnetic field, the maximum current of the accelerated electron can be calculated using Alfven’s current according to Molokovsky and Sushkov [41].

$$I \leq I^A = 1.7 \times 10^4 \gamma v / c \quad (2.7)$$

$$\gamma \cong 1 + (1.96 \times 10^{-6}) U_a \quad (2.8)$$

$$v \cong (5.95 \times 10^5 / \gamma) \sqrt{U_a (\gamma + 1) / 2} \quad (2.9)$$

$$\therefore I \leq 33.7 \sqrt{U_a} \quad (2.10)$$

Where, I is the current of the emitted electron and I^A [A] represents the Alfven's current. From Eq. (2.8), U_a [V] is the accelerating voltage of the emitter. When the accelerating voltage is under magnitude of 4, the relativistic factor can be approximated to be '1'. Representing the maximum current equation by the function of the accelerating voltage, the energy density in central place can be estimated using the relation of ' $P = VI$ '.

$$E_{d0} = P\tau / S = U_a I\tau / S \quad (2.11)$$

$$\therefore E_{d0} \leq 33.7\tau(U_a)^{3/2} / (\pi r^2) = \eta 33.7\tau(U_a)^{3/2} / (\pi r^2) \quad (2.12)$$

Where, E_{d0} [J/cm²] is the energy density at the center, P [W] means the power. Then, τ [s] is irradiation duration and S [cm²] is stand for the area of electron beam. r [cm] is the radius of electron beam. In an ideal case, the energy density can be estimated by applying the Alfvan's current equation. Therefore, it is approximated that the energy density is mainly affected by the accelerating voltage. η is the efficiency for considering the real system. Following Rehn et al. [42], White and Aziz presented the energy loss model in penetration depth direction, which is estimated by Gaussian distribution.

$$E_d(z, t) = E_{d0}(t)(1 - \beta) \exp[-(z - z_p)^2 / (2\sigma^2)] \quad (2.13)$$

$$z_p = (143Z + 622)r_0 \quad (2.14)$$

$$\sigma = (-538 \ln Z + 3740)r_0 \quad (2.15)$$

$$r_0 = AE_{d0}^a \quad (2.16)$$

$$A = 3.92 \times 10^{-6} + 1.562 \times 10^{-7} Z \quad (2.17)$$

$$a = 1.777 - 2.165 \times 10^{-3} Z \quad (2.18)$$

Where, β is the energy reflection coefficient or so called backscattering coefficient and z_p [μ m] is the maximum absorptivity depth. σ [μ m] is the standard deviation of absorbed electron location and Z is

the atomic number. The parameter of penetration range (r_0) can be obtained from the Eq. (2.16). A and a are just fitting parameters for experimental results. Composed the all above equations, the appropriate PEB energy generation model at central position is can be completed. In Chapter 3, additional modelling and verification of the machine used in this thesis are discussed.

Figure 2-5 shows schematic of pulsed electron beam equipment. According to Proskurovsky et al. [43], the first equipment applying PEB technology is introduced in Russia. The first equipment model ‘Nadezhda’ series is invented for using ‘EEE’ effects. Specifically, the EB source is called ‘low-energy high-current electron beam (LEHCEB)’, many researches for surface modification of iron, Ti-alloys, Al-alloys and Ni-alloys are proposed using this machine. Then, at the almost same period, the new type of the PEB machine is created in named for ‘Gepulste ElektronStrahl Anlage (GESA)’ series in Germany by Engelko et al. [44]. Due to the machine is designed to vertical structure not horizontal, this machine can be adapted more conventionally. Also, similarly, in France and China, ‘HOPE’ series are development purposed to be surface treatment equipment. The EB source of GESA and HOPE is called ‘high-current pulsed-electron beam (HCPEB)’. More recently, in Japan, Uno et al. [11] introduce the new PEB surface treatment machine. This is called ‘Electron Beam PIKA Finish Machine (PIKA series, model: PF32B)’ produced by ‘Sodick’. They named the EB source is ‘large pulsed electron beam (LPEB)’. The detailed of this machine is well discussed in Chapter 3.

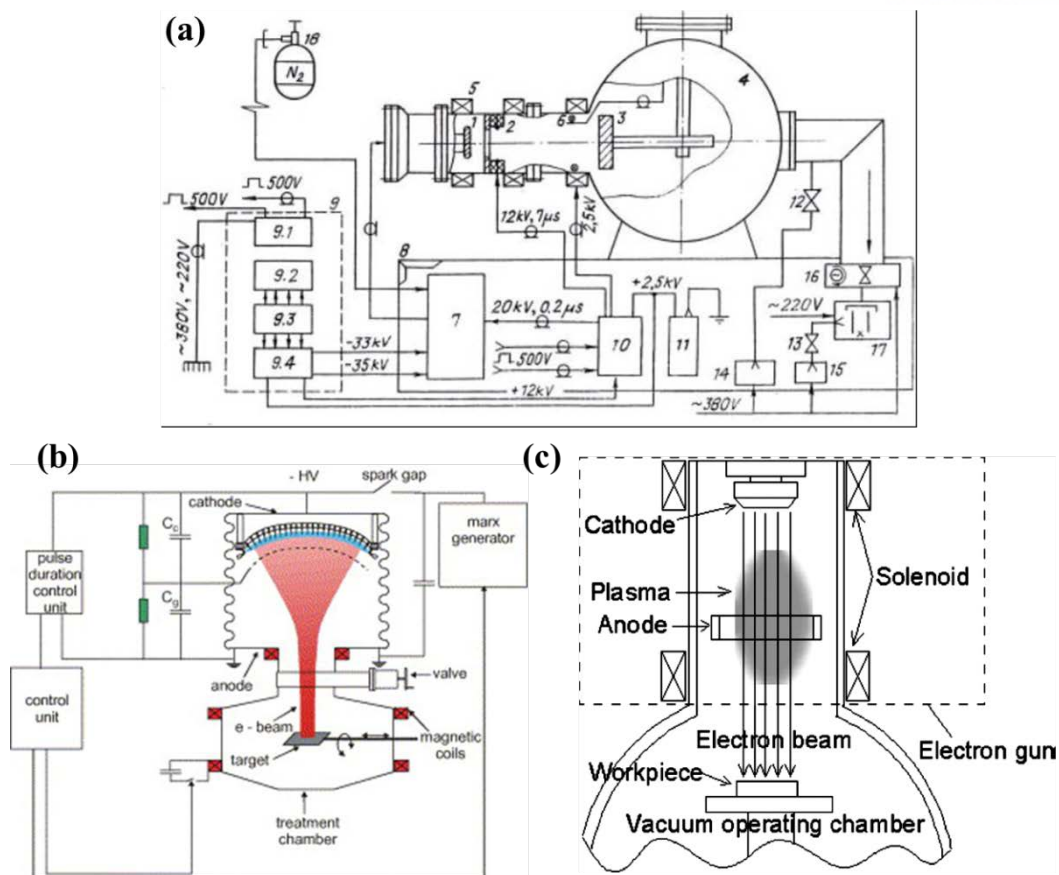


Figure 2-5. Schematics of the different types of PEB machine; (a) Nadezhda [36], (b) GESA [44], and (c) PIKA [11].

2.2.2. Surface modification by electron beam irradiation

In this section, the published PEB surface modification researches are briefly discussed focused on the change of corrosion properties about the typical 4 metallic materials such as steel, Al-, Ti-, and Mg-alloys. Firstly, PEB is generally used to mold steel for fabricating hardened surface layer. Zhang et al. [45] investigated the surface modification of AISI 304L austenitic stainless steel using HCPEB in the view of corrosion resistance. They showed that the pitting corrosion decreases on the surface immersed in seawater with increase EB pulses. The EIS measurement proved that the corrosion resistance is mostly doubled from $\sim 31 \text{ k}\Omega\cdot\text{cm}^2$ to $\sim 62 \text{ k}\Omega\cdot\text{cm}^2$ after 10 pulses. Also, Kim et al. [46] studied the surface modification of mold steel materials applying LPEB. Surface quality and glossiness of KP1, KP4 are remarkably improved using $10 \text{ J}/\text{cm}^2$ energy density. For example, the corrosion rate of KP4 is decreased from $0.01688 \text{ mm}/\text{y}$ to $0.00809 \text{ mm}/\text{y}$ as a result of potentiodynamic polarization test in 1 wt.% NaCl solution.

Next, the surface modification results of Al-alloys with HCPEB are reviewed by Rotshtein et al. [47]. The electrochemical impedance of Al6061 alloy is improved by HCPEB irradiation from 3 degree of decade to 5 degree of decade resistance level ($\Omega \cdot \text{cm}^2$). They suggested that the enhancement is owing to the protective Al_2O_3 film formed after irradiation and second-phase particles under pulsed melting. For Ti-alloys, Walker et al. [48] showed that the corrosion behavior of LPEB irradiated Ti-6Al-4V surfaces. OCP measurements and cyclic polarization curves in 3.5 wt.% NaCl solution supported that the corrosion rate is decreased from 923.2 to 5.478 nm/y. In the case of 15 and 25 LPEB pulses on Ti-alloys, a homogenous α' -martensitic surface layer was fabricated within prior β -grain boundaries by twinning and slips. Similarly, Kim et al. [49] asserted that LPEB can improve the overall surface qualities of Ti-6Al-7Nb. From the results of EIS measurement in 1 wt.% NaCl solution, the corrosion impedance is increased from ~ 170 to $\sim 260 \text{ k}\Omega \cdot \text{cm}^2$ in the 10 J/cm^2 energy density used samples.

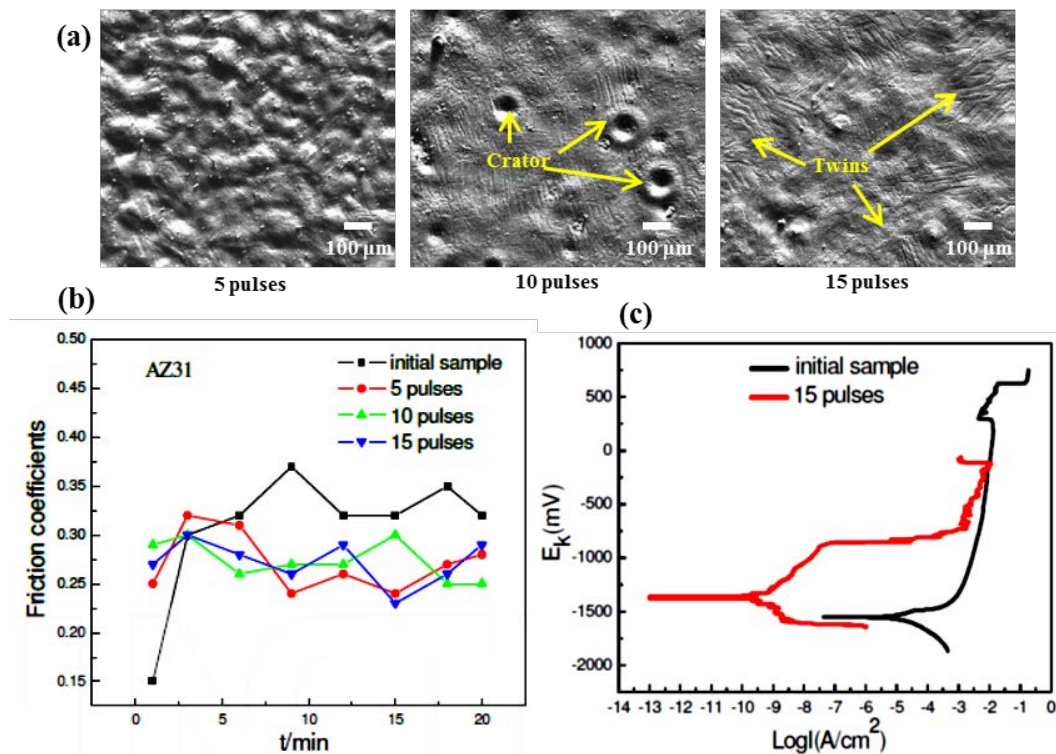


Figure 2-6. (a) Surface SEM morphologies of AZ31 Mg-alloy after HCPEB irradiation with different pulses, (b) Evolution of friction coefficients with friction time, and (c) Potentiodynamic polarization curves of AZ31 before and after HCPEB treatment (15 pulses) [36].

Lastly, the PEB treated Mg-alloys are also investigated by many researchers. According to Bo et al. [36], the surface of AZ31 can be enhanced by HCPEB (3 J/cm^2). The EB process evaporated the Mg selectively in Mg-Al binary allotropic system. From Figure 2-6 (a), the surface morphology can be analyzed. Craters are generated at 10 pulses and twining structure is also detected at 15 pulses. The Al-enriched surface shows a nobler wear and corrosion resistance than the bare surface. It is given at Figure 2-6 (b), the friction coefficient is slightly decreased on the HCPEB treated surface. Then, Figure 2-6 (c) shows that the corrosion potential is increased and corrosion current is reduced (polarization test in 5 wt.% NaCl solution). They stated that the rapid quenching ($\sim 10^8 \text{ K/s}$) by HCPEB builds stable crystal grain structure and reduces the proportion of anode and cathode causes galvanic corrosion. Most recently, Hao & Li [5] (Figure 2-7) reported article using HCPEB (3 J/cm^2) for increasing microhardness of AZ91 from 62.7 HK to 141 HK. And it is reported that corrosion current (polarization test in 3.5 wt.% NaCl solution) is reduced by two orders of magnitude. According to the EDS results, Al contents of the HCPEB treated surfaces ($\sim 8 \text{ }\mu\text{m}$ thin-film) is increased from $\sim 9 \text{ wt.}\%$ to more than $30 \text{ wt.}\%$. Then, through the XRD results, it is shown that Mg is selectively vaporized by electron beam heating on the original grain structure with $\alpha\text{-Mg}$ (hcp) having weak slip plane and relatively rich Al is alloying with Mg newly converted to nano-grained metastable phase $\text{Mg}_{3.1}\text{Al}_{0.9}$ and strong grain structure $\beta\text{-Mg}_{17}\text{Al}_{12}$ formed is suggested to the main reason for the improvement.

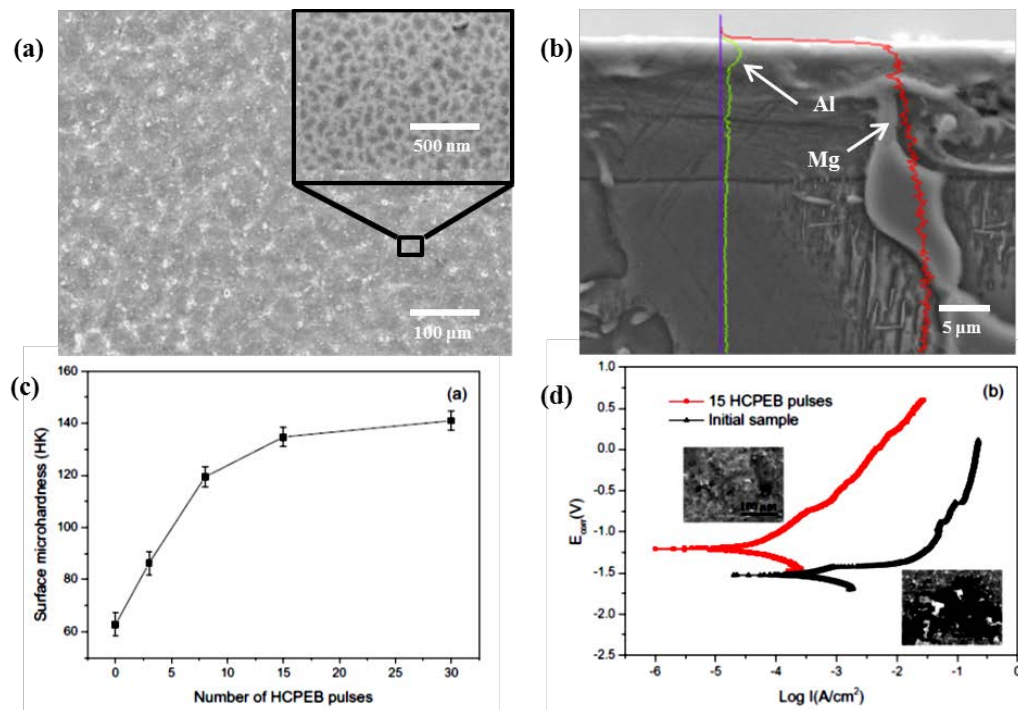


Figure 2-7. (a) HCPEB treated surface of AZ91, (b) EDS result of cross-section, (c) Microhardness modification through number of pulses, and (d) Polarization curve [5].

Table 2-2. Literature review of pulsed electron beam surface treatment on Mg-alloys.

Mat.	Y.	Authors (country)	Equipment	Parameters	Results
AZ91	16	Hao & Li [5] (China)	HCPEB (HOPE-I)	3 J/cm ² (27 kV, 0.007 Pa, 2.5 us), 15 pulses	Metastable $\alpha+\beta$ Mg _{3.1} Al _{0.9} layer, nano-hardness, corrosion resistance improve
AZ91	14	Li et al. [6] (China)	HCPEB (HOPE-I)	3 J/cm ² (27 kV, 0.007 Pa, 2.5 us),	Nano-grained $\alpha+\beta$ Mg _{3.1} Al _{0.9} layer, corrosion resistance improve
AZ91	09	Li et al.[7] (China)	HCPEB (Nadezhda-2)	2.5 J/cm ² (27 kV, 0.009 Pa, 1 us),	β -Mg ₁₇ Al ₁₂ layer, wear resistance improve
AZ91	07	Gao et al. [8] (China, France)	HCPEB (Nadezhda-2)	3 J/cm ² (1 us), Ø60 mm, 15 pulses	Nano-grained α -MgO, Al- enriched layer, wear and corrosion resistance improve
AZ31	11	Bo et al. [36] (China, France)	HCPEB (Nadezhda-2)	3 J/cm ² (1 us), Ø60 mm, 15 pulses	Al-enriched layer, wear and corrosion resistance improve
AZ31	05	Gao et al. [10] (China, France)	HCPEB (Nadezhda-2)	2.5 J/cm ² (1 us),	Al, Mn-enriched layer, micro- hardness, wear resistance improve

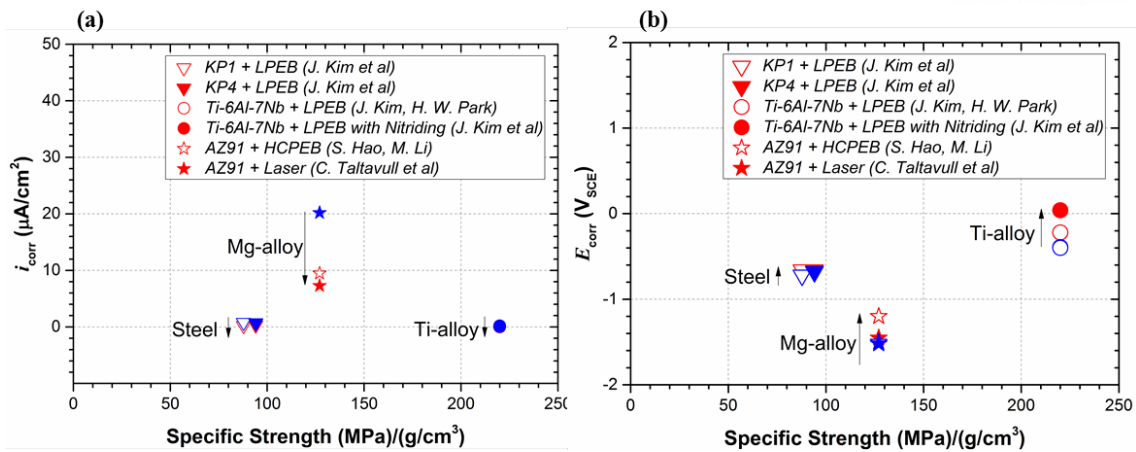


Figure 2-8. Result comparisons of (a) corrosion current density, (b) corrosion potential of steel, Ti-alloy, and Mg-alloy in potentiodynamic polarization analysis [5, 38, 46, 49, 50].

Figure 2-8 shows a several corrosion analysis results of the metallic alloys surface treatment among the direct energy beam irradiation process. In the polarization diagram, the corrosion current of Mg-alloy is remarkably improved rather than other materials, which associate with the corrosion rate. However, the corrosion potential is increased not so much, which represent originally poor at cathodic ionization of Mg-alloys rather than other metallic alloys.

2.3. Summary

Based on the literature reviews relating to the surface treatment of Mg-alloy, surface modification by electron beam irradiation, the researches on corrosion resistance enhancement has been summarized in this chapter. From now on, CVD, PVD, ion beam, laser, and EB are applied for improving the surface hardness, wear/corrosion resistance of Mg-alloys. The mechanism of PEB irradiation is explained by dynamics with electromagnetic forces in vacuum and electron beam energy absorption distribution for each material property. Most of studies on the PEB surface treatment of Mg-alloys have reported the effect of parameters on fabrication of the protective re-crystallization layer produced by HCPEB (2.5 - 3 J/cm², 10 - 15 pulses) process. They tried to explain the evaluation of corrosion using 3-electrode cell tests (potentiodynamic polarization curve, EIS measurement).

III. Surface modification of Mg-alloys using a large pulsed electron beam irradiation

The surface modification of Mg-alloys is activated by electrical power using pulsed electron beam equipment. The mechanism of the EB surface treatment can be modeled by heat diffusion equation. The effects of LPEB process can be checked in macro scale. However, to analysis the surface modification phenomenon in micron level, it is required to investigate the energy absorption model affected by the atomic number of the working material and the parameters of LPEB process. Therefore, the mathematical modeling procedure is detailed described in this chapter. Then, using FDM simulation, the temperature profile is predicted and certified by the experimental results. Also, the entire experimental set up and the results of the mechanical and electrochemical characteristics analysis are also included in this chapter.

3.1 Simulation of a large-pulsed electron beam irradiation

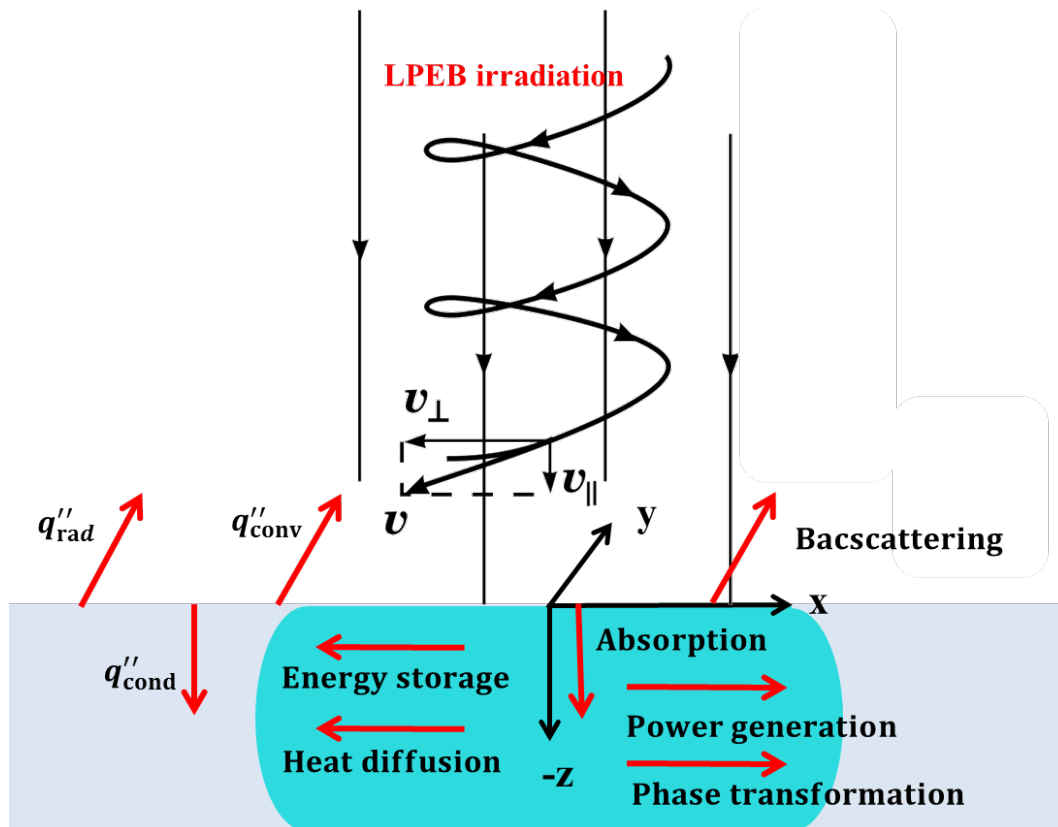


Figure 3-1. Schematics of heat transfer mechanism when LPEB irradiation.

In this section, in order to anticipating heat treatment process appropriately, it is compromised to mathematical modeling of the energy density absorption distribution profile of the LPEB process which is for the simulation of ‘Electron Beam PIKA Finish Machine (PF32B)’. Figure 3-1 presents a heat transfer elements of LPEB irradiation. In the energy conservation equation (Eq. (3.1)), the heat source (S_H [W/m^3]) is modeled by electron beam energy distribution at the heating process. The all modeling process is conducted by MATLAB and the non-linear calculation is solved by finite difference method (FDM). The governing equation is expressed as:

$$S_H = -\nabla(k\nabla T) + \rho(c_p \frac{\partial T}{\partial t} + \frac{\partial H_F}{\partial t}) \quad (3.1)$$

$$H_F = \begin{cases} 1 & T > MP \\ L_F \cdot \frac{T - FP}{MP - FP} & FP \leq T \leq MP \\ 0 & T < FP \end{cases} \quad (3.2)$$

Where, k is the thermal conductivity, ρ is the density, and c_p is the specific heat (constant pressure) of the working material. The governing equation contains heat source in external term. The heat diffusion and storage elements with enthalpy of phase transformation are included in internal term. H_F is the enthalpy of fusion, L_F is the latent heat of fusion, FP and MP means each freezing point and melting point. The latent heat generation can be applied at the state of phase transformation using enthalpy form Jamshidinia et al. [51]. Because of the melting temperature of Mg-alloy are relatively low, the phase transformation element is very important to analysis of the temperature profile. The initial temperature (T_0) and the maximum temperature (T_{max}) are expressed by that:

$$T_0 = ST \quad (3.3)$$

$$T_{max} = EP \quad (3.4)$$

Where, ST is service temperature in vacuum chamber, which is generally similar with a room temperature ($27^\circ C$). EP is the evaporation point. If the surface temperature reaches at the evaporation point, it is vaporized and the debris contaminates the vacuum chamber. However, in this FDM simulation, the evaporation mechanism was not considered because it makes the calculation too complicate. The boundary conditions are given that:

At the surface:

$$P_d = -k \frac{\partial T}{\partial z} + \frac{\rho dz}{2} \left(c_p \frac{\partial T}{\partial t} + \frac{\partial H_F}{\partial t} \right) + h(T - T_\infty) + \varepsilon \sigma_r (T^4 - T_{\text{surr}}^4) \quad (3.5)$$

At the side:

$$T = \frac{\sqrt{(k\rho c_p)_A} T_A + \sqrt{(k\rho c_p)_B} T_B}{\sqrt{(k\rho c_p)_A} + \sqrt{(k\rho c_p)_B}} \quad (3.6)$$

For the boundary, the power density P_d [W/m^2] is applied at the surface. Then, h means the coefficient of convection, ε equals the emissivity, and σ_r is Stefan-Boltzmann constant (5.67×10^{-8} [$\text{W}/(\text{m}^2 \cdot \text{K}^4)$]) for radiation. T_∞ and T_{surr} means each the ambient and the surrounding temperature in the vacuum chamber. The electron beam is pulsed for each 10 seconds, but the pulse duration time is only 2 μs . Therefore, in the rest time, the heat loss with convection and radiation is to be mainly considered. However, since the convection coefficient is generally very small at the vacuum condition, it was ignored. Also, even though the emissivity is dependent parameter, it was fixed at the constant value '0.3'. Then, at the side, the diffusion process is activated by a steel zig. In this study, it was simplified by the semi-infinite conduction at the between the two materials. T_A and T_B is the temperature of the different two materials.

$$S_H = P_d / COE = E_d(x, y, z, t) / (\tau \cdot COE) \quad (3.7)$$

$$E_d(x, y, z, t) = nE_d(z, t) \exp[-n(x^2 + y^2) / (\varepsilon r)^2] \quad (3.8)$$

$$E_d(z, t) = E_{d0}(t)(1 - \beta) \exp[-(z - z_p)^2 / (2\sigma^2)] \quad (3.9)$$

$$\therefore E_{d0} = \eta 33.7 \tau (U_a)^{3/2} / (\pi r^2) \cong \eta \times 2.38 \times 10^{-6} (U_a)^{3/2} \quad (3.10)$$

From the Goldak's semi-ellipsoidal heat source model (Goldak et al. [52]), the energy density of electron beam can be estimated by a normal distribution. Where, COE is center of energy absorption distribution. n and ε are adjustable values for adapting to Gaussian distribution. By synthesizing the z -depth direction energy distribution and Goldak's semi-ellipsoidal heat source model, the semi-spherical shape of Goldak's model can be formed. The model of the energy density at the center can be obtained from the given White & Aziz absorption model [42]. Therefore, based on the reported relations of the energy density, the LPEB heat transfer model can be obtained. Most of all, the LPEB energy density at the center can be figure out with the accelerating voltage. The beam radius of LPEB is 3 cm and the pulse duration time of LPEB is 2 μs .

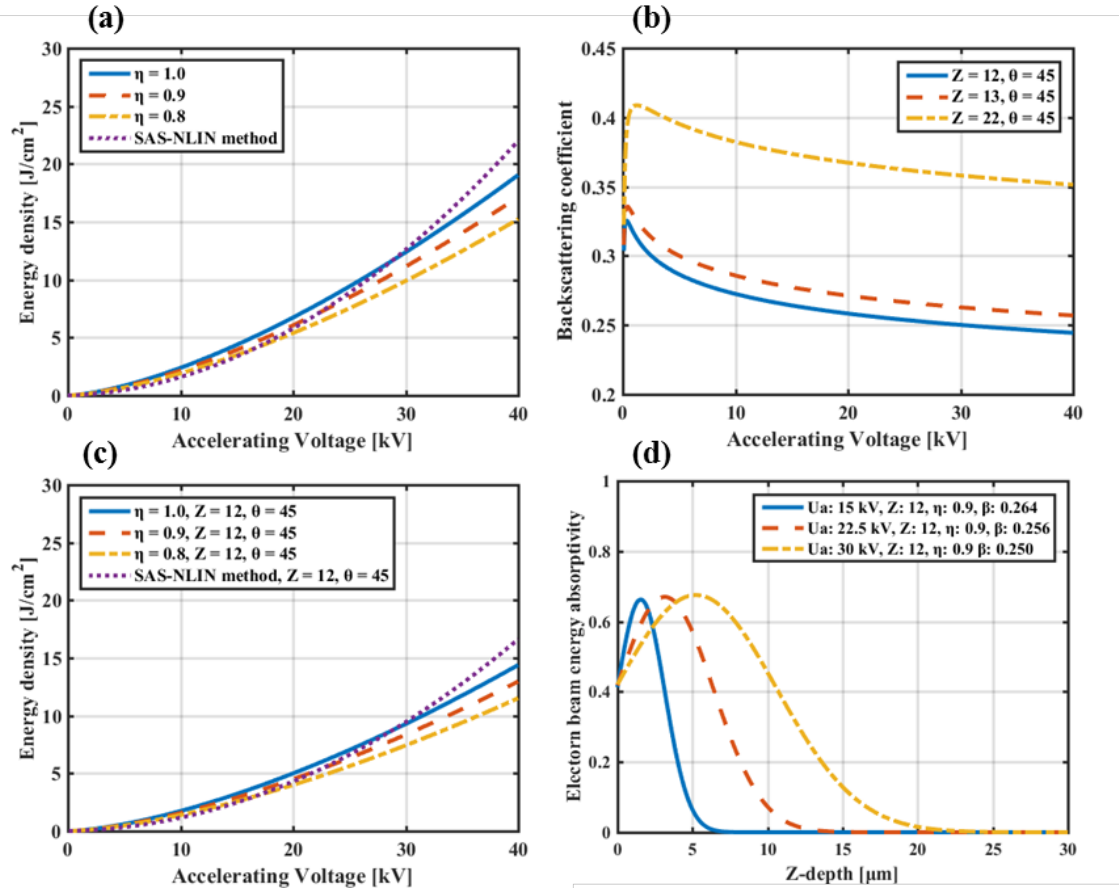


Figure 3-2 (a) LPEB energy density at the center with accelerating voltage, (b) backscattering coefficient at different atomic number, (c) characteristic curve of energy density, and (d) electron beam energy absorptivity in magnesium with different accelerating voltage.

The Figure 3-2 shows Alfvan's current model is well-matched with SAS-NLIN method [13] at η is ~ 0.9 in the range of 15 - 30 kV. The error is result from the difference of ideal and real electromagnetic forces in vacuum condition. Also, the backscattering effect has an effect on the experimental value. The backscattering coefficient (β) was suggested by Staub method [53].

$$\beta = \beta_0^{1-\kappa(1-\cos(\theta))} \quad (3.11)$$

$$\beta_0 = B(1 - \exp(-0.0066B^{-2.5Z})) \quad (3.12)$$

$$\kappa = 1 - \exp(-1.83U_a^{0.25}) \quad (3.13)$$

$$B = 0.4 + 0.065 \ln(U_a) \quad (3.14)$$

Where, β_0 is backscattering coefficient when the electron beam irradiation path is not inclined. κ and B are the fitted parameters by experiment. θ means the angle of electron beam irradiation on the surface. Since the LPEB has spiral path, the θ is to be assumed at 45 degrees. The Figure 3-2 (b) shows the curve of backscattering coefficient. It is increased proportional to atomic number (Z). The backscattering coefficient of Mg-alloy is 0.25 – 0.27 in the region of interest for accelerating voltage. The modified model of electron beam energy density with backscattering effect is given at Figure 3-2 (c) The theoretical model shows that 3, 5, 10 J/cm² energy density of LPEB can be realized using each 15, 22.5, 30 kV accelerating voltage with η is 0.9. The depth profile of energy absorptivity is depicted at Figure 3-2 (d) using the Eq. (3.9).

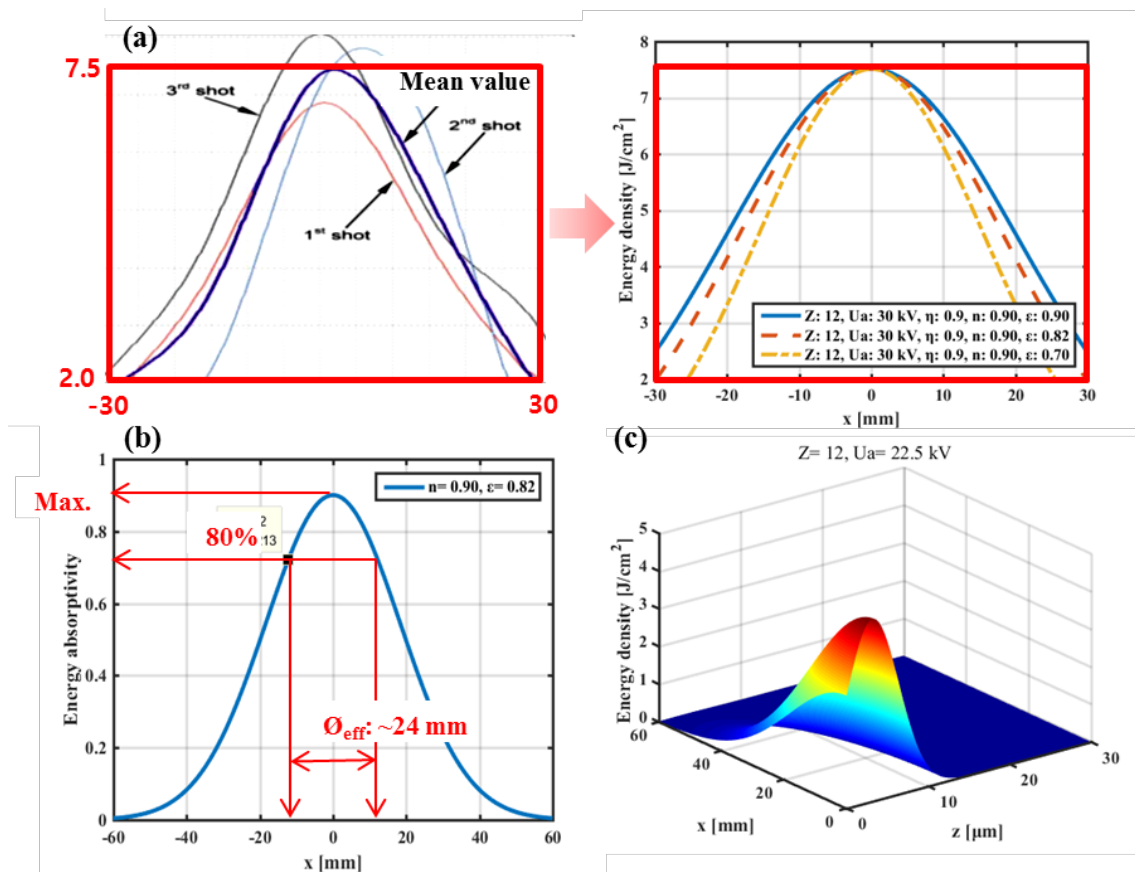


Figure 3-3. (a) Gaussian distribution to the X-Y direction; the left graph is the experimental results and the right graph is the approximation result, (b) energy absorptivity of lateral direction, and (c) 3D energy absorption distribution of electron beam.

Figure 3-3 (a) indicates fitting lateral energy distribution of LPEB. To modelling, the experimental results of Daichi et al. [13] were used. The shape is possible to be fitted by Gaussian distribution. From the Eq. (3.8), when the adjustable parameter n is 0.90, the effectiveness of beam radius ε was selected to 0.82. The result of lateral energy absorptivity is given at Figure 3-3 (b). The range is preserved at least 80% of the maximum value at the center is called effective beam diameter (\varnothing_{eff}), which was ~ 24 cm in this model. Consequently, Figure 3-3 (c) presents the three-dimensional energy density profile of LPEB when the material is Mg and accelerating voltage is 22.5 kV ($E_d \doteq 4.8 \text{ J/cm}^2$ at the center of the maximum absorption depth).

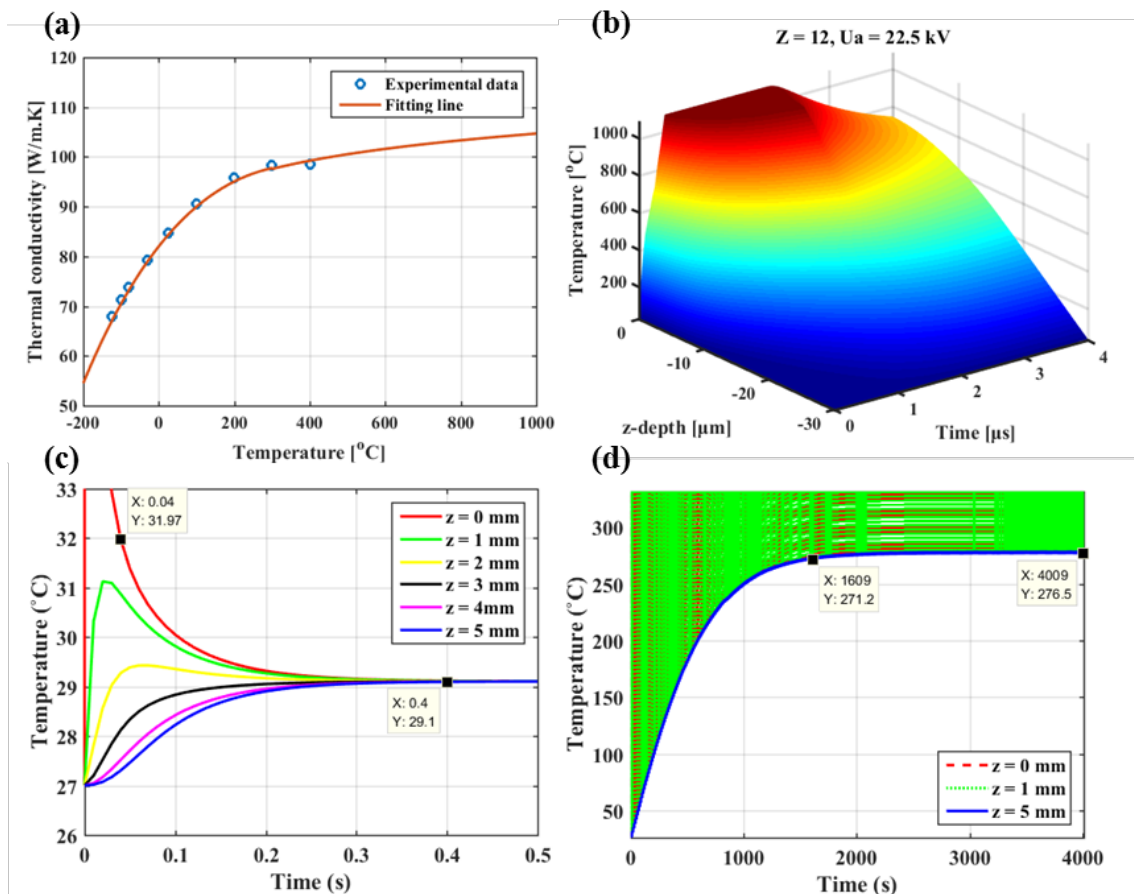


Figure 3-4. (a) Thermal conductivity of AZ31 [54], (b) Temperature profile of LPEB irradiation of AZ31, (c) the single pulse of LPEB process, and (d) the multi pulses of LPEB process.

From Lee et al. [54], the thermal properties of AZ31 can be identification like Figure 3-4 (a). Figure 3-4 (b) shows a result of AZ31 temperature profile by FDM simulation, which is progressed using 2D backward difference scheme ($x_{\max} = 20$ mm, $z_{\max} = 5$ mm, and $t_{\text{final}} = 10$ s) with $Fo < 1/4$. It is perceived that the heating curve is delayed at the melting point. The melting depth is estimated to ~ 10 μm when the accelerating voltage is 22.5 kV. And the temperature of 4 μm depth region is increased up to the evaporation point per each pulse. For this reason, the real re-solidified layer is approximated to be 6 - 10 μm . Figure 3-4 (c) shows the profile of temperature change in the top surface, 1 mm depth, and the bottom. The temperature is abruptly declined as the rate of 2.6×10^4 K/s. Then, the temperature is ascended by 2.1 K per one LPEB pulse in all region of the material, finally it is converged at 270 - 280 $^{\circ}\text{C}$ when over 160 pulses shown at Figure 3-4 (d). Generally, Porter et al [55] presents the Mg-alloy is quenched to a temperature of 220 $^{\circ}\text{C}$ for 20 min followed by 90 s at 277 $^{\circ}\text{C}$ and finally water quenched for heat treatment. The eutectic solidification is activated by the high temperature at which the total driving force of transformation is declined. Therefore, the free energy, necessary to form α/β interfaces, is lowered. However, the number of pulses should be delicately controlled in order to consider the appropriate heat treatment performance with shape deformation because the evaporated region is continuously overlapped by the LPEB pulses.

3.2. Experimental setup

3.2.1. Material

The sample is square (40 mm by 40 mm by 5 mm) shaped and the surface is well polished ($\sim 5 \mu\text{mRa}$) by the mechanical tools. When machining process, it is cautious that the powder of Mg is easily exploded if it reacts with water. Then, the surface is rinsed by ethanol. The chemical composition of the materials (AZ31, AM60, and AZ91) is displayed at [Table]. In this study, AZ31 is selected to the target material because its Al content is the least among them and its mechanical property is superior to the other. Also, AZ31 is well-matched the objectives of the LPEB process, which is increasing the surface Al content compared to the substrate for engineering application. AZ91 and AM60 samples were used for verifying the effects of surface modification. The all samples are provided from Korea testing & research institute (KTR).

3.2.2. Surface treatment

The photograph with schematics of ‘electron beam PIKA finish machine’ is depicted at Figure 3-5 with the LPEB process conditions are suggested at Table 3-2. The Figure 3-5 (a) shows an image of the machine of LPEB process (model: PF32B), which is located at ‘MakeLAB’ in UNIST. The main three parameters of LPEB process are the energy density, the irradiation pattern, and the number of cycles. To find the optimum parameters of LPEB surface treatment for AZ31, many tests are accompanied by trial and error. Then, it reduces the redundant cases simultaneously. Also, although the pulse duration is fixed at only $\sim 2 \mu\text{s}$, the machine can provide freely energy density up to 10 J/cm^2 to control the accelerating voltage at the cathode. Therefore, this machine can provide a larger electron beam energy density than HCPEB. To keep on the electron beam accelerating mechanism, the working chamber should be sustained a high vacuum state to be enable for plasma generation. In this experiment, the vacuum pressure is controlled by 0.05 Pa, which is displayed at Figure 3-5 (a). The plasma gas is argon (Ar). As shown that Figure 3-5 (b) the sample both end sides are fixed by a steel zig attached in the vacuum chamber and the bottom surface is completely detached. The irradiation pattern of LPEB is presented at Figure 3-5 (c). Considering the square-shaped Mg-alloy sample and the effective beam diameter, the pitch of stitching is determined to 20 mm and the stage is moved at 2 by 2 points using the LM guide and NC control. Hence, the 1 cycle is composed of 4 LPEB pulses in this experiment. Since the single LPEB pulse can be irradiated per 10 - 20 s and the total vacuum adjusting time is $\sim 12 \text{ m}$, the 40 cycles of LPEB process takes approximately 52 m.

Table 3-1. Material's chemical composition

wt. %	Mg	Al	Zn	Mn	Si	Ca	Fe	Cu	Ni	Others
AZ91	Bal	8.3-9.7	0.35-1.0	0.15	0.10	-	0.005	0.030	0.002	0.02
AM60	Bal	5.5-6.5	0.22	0.25	-	-	0.005	0.010	0.002	0.003
AZ31	Bal	2.5-3.5	0.7-1.3	0.20	0.10	0.04	0.005	0.04	0.005	0.30

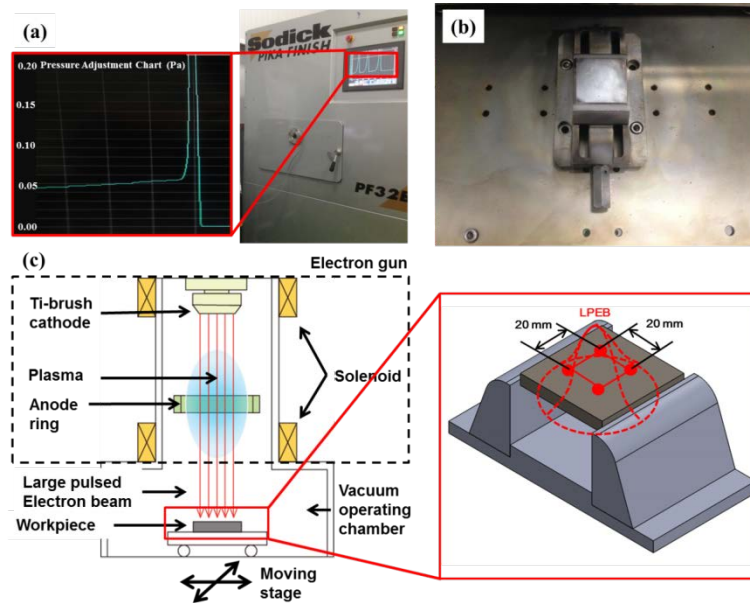


Figure 3-5. (a) Graphics of PIKA Finish Machine, (b) Set-up of LPEB process, and (c) Schematics of LPEB surface treatment process.

Table 3-2. LPEB process parameters.

Parameter (unit)	Value
Energy density (J/cm^2)	3, 5, 7, and 10
Pulse duration (μs)	~2
Period (s)	10 - 20
Beam diameter (mm)	60
Irradiation pattern	2 by 2
Pitch (mm)	20
Number of cycles	1, 10, 20, 40, and 100
Irradiation distance (mm)	30
Vacuum pressure (Pa)	0.05

3.2.3. Other equipment

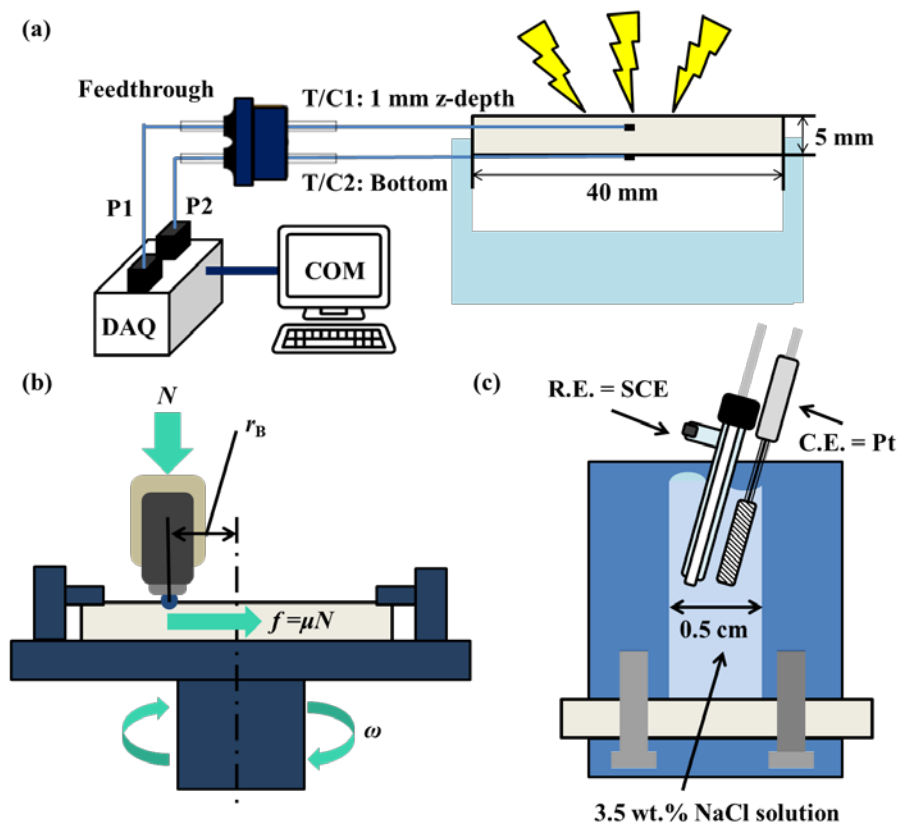


Figure 3-6. Schematics of (a) the temperature monitoring system, (b) the ball-on-disc wear test system, and (c) the 3-electrode cell test system.

[1] Temperature measurement

The temperature is measured by using K-type thermocouple. Specification of K-type thermocouple is that the operating range is from -50°C to 500°C , and the sampling time is almost 1 second. Figure 3-6 (a) shows the location and wire connection of the temperature sensor. It is connected to the between the thermocouple and DAQ using feedthrough. The model of DAQ is 'NI 9263', and the software is 'LabVIEW 2011 Version' which is used for signal processing. It is cautious that the measurement environment is very harsh because the high voltage electron beam pulse is far danger. Therefore, the over fluxed LPEB pulses can interfere with the temperature monitoring system when the temperature of the device is increased over a degree of the limit.

[2] Surface profile measurement & Ball-on-disc wear test

The surface roughness can be measured by ‘Semi Auto Formtracer System (model: 525-421k-1)’. Also, the main purpose of 3D mapping using ‘Coordinate Measuring Machine (model: PGS)’ is checking the deformation of LPEB surface modification process. To measure the height of the sample accurately, a reference of the sample is fixed at the same point. The test is repeated at least 3 times. Then, the precision is 0.1 micron. ‘3D Formtracer (model: NV 3000)’ is also used for checking the 3D surface profile. Above all equipment is placed at ‘MakeLAB’ in UNIST.

The device of ball-on-disc wear test is depicted at Figure 3-6 (b) which machine (model: UMT-2T) is installed at ‘MHMLAB’ in UNIST. This machine can measure the coefficient of friction during the rotational motion of the ball-on-disc. The normal force and the rotational speed with radius of the ball are the parameters of this test. The experiment is accomplished for checking the mechanical properties by the modification of LPEB treated sample. The weight loss and the height of the wear track were also measured.

[3] 3-electrode cell test

The electrochemical properties were evaluated by the 3-electrode cell test in 3.5 wt.% NaCl solution. Figure 3-6 (c) presents the configuration for potentiodynamic polarization and electrochemical impedance spectroscopy (EIS). ‘IviumStat’ is used for the potentiostat device with the software of ‘IviumSoft’ and ‘ZView’. The apparatus is provided in UNIST. In this experiment, the LPEB treated Mg-alloy samples were used for working electrode. The reference of the cell is applying a standard calomel electrode (SCE) and the counter electrode is set to platinum. The measurement system can provide an ability to cover the -10 to 10 V range of DC voltage and micro current (-5 to 5 A) signal sensing as well as a high frequency (10 μ Hz - 8 MHz) AC signal input and output. It can provide to not only evaluate the corrosion-protecting performance qualitatively, but also analyses the information quantitatively by linear polarization method and equivalent circuit modeling.

The potentiodynamic polarization is DC method for measuring the steady-state current by linear potential variation. In this study, the scan rate of the applied potential is 10 mV/s. Using low-field approximation at the polarization curve, the Stern-Geary equation (Eq. (3.15)) can be estimated from Butler-Volmer equation. And, the corrosion penetration depth rate (v_{corr}) can be calculated by the Eq. (3.16).

$$R_p = \frac{1}{2.303} \frac{\beta_a \beta_c}{(\beta_a + \beta_c)} \frac{1}{i_{\text{corr}}} \quad (3.15)$$

$$v_{\text{corr}} = \frac{A}{z_k F \rho} i_{\text{corr}} \quad (3.16)$$

Where, R_p is polarization resistance, β_a and β_c is each anodic and cathodic Tafel slop. The slop can be obtained by nomogram method. Then, A_w is atomic weight, z_k is charge number of the metallic ion, and F is Faraday constant (96500 [C/mol]). The v_{corr} is just another expression of i_{corr} for engineering application.

Then, EIS is AC method by identifying the impedance applying frequency analysis, which is enabled by comparing the sinusoidal voltage input and output pass through the system. In this experiment, the amplitude of the oscillation is 1 V and the frequency is scanned from 200000 Hz to 0.2 Hz. The amplitude is selected to larger value than the preferred condition (< 5mV). Since the small perturbation implies a linear relation of current density versus potential, the Eq. (3.15) can be applied to the experiment by assuming the charge transfer resistance (R_{ct}) obtained value from the impedance plot is equal to the polarization resistance. For this reason, the large amplitude value can cause an error of the fundamental modeling but, in order to eliminating a white noise, it was indispensable. The corrosion test is repeated at least 3 times per one sample.

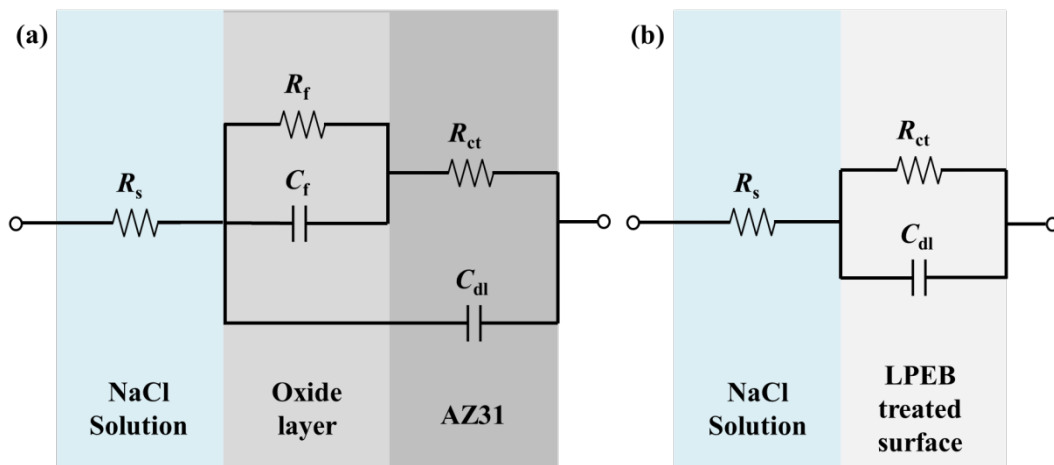


Figure 3-7. The equivalent circuit model of (a) bare surface and (b) LPEB treated surface.

Figure 3-7 shows the modeling elements of electrochemical system. At the redox surface, charge transfer phenomenon of metallic materials is happened in ionic solution. Mostly, the system of the electrochemical reaction can be expressed by 2nd order equivalent circuit model. At Figure 3-7 (a), where, R_s is solution resistance, R_f means film resistance which is the represent of oxide layer, and the double layer capacitance in the film was modeled by C_f . The R_{ct} is charge transfer resistance of the bare AZ31, and the C_{dl} is the double layer capacitance of the total redox surface as a phase shift element. After LPEB process, it is transformed a 1st order equivalent circuit model as shown to Figure 3-7 (b) because the oxide layer is entirely eliminated by LPEB irradiation. However, the LPEB treated surface can be modelled by more stable impedance elements with the modified R_{ct} and C_{dl} . The equivalent circuit modeling is practiced to EIS data by curve fitting process. In this process, the charge phase element (CPE) is used for modeling of the C_{dl} with depression parameter (n) and Q such that:

$$Z(CPE) = (j\omega)^{-n} / Q \quad (3.17)$$

3.3. Results and discussion

3.3.1. Temperature profile analysis

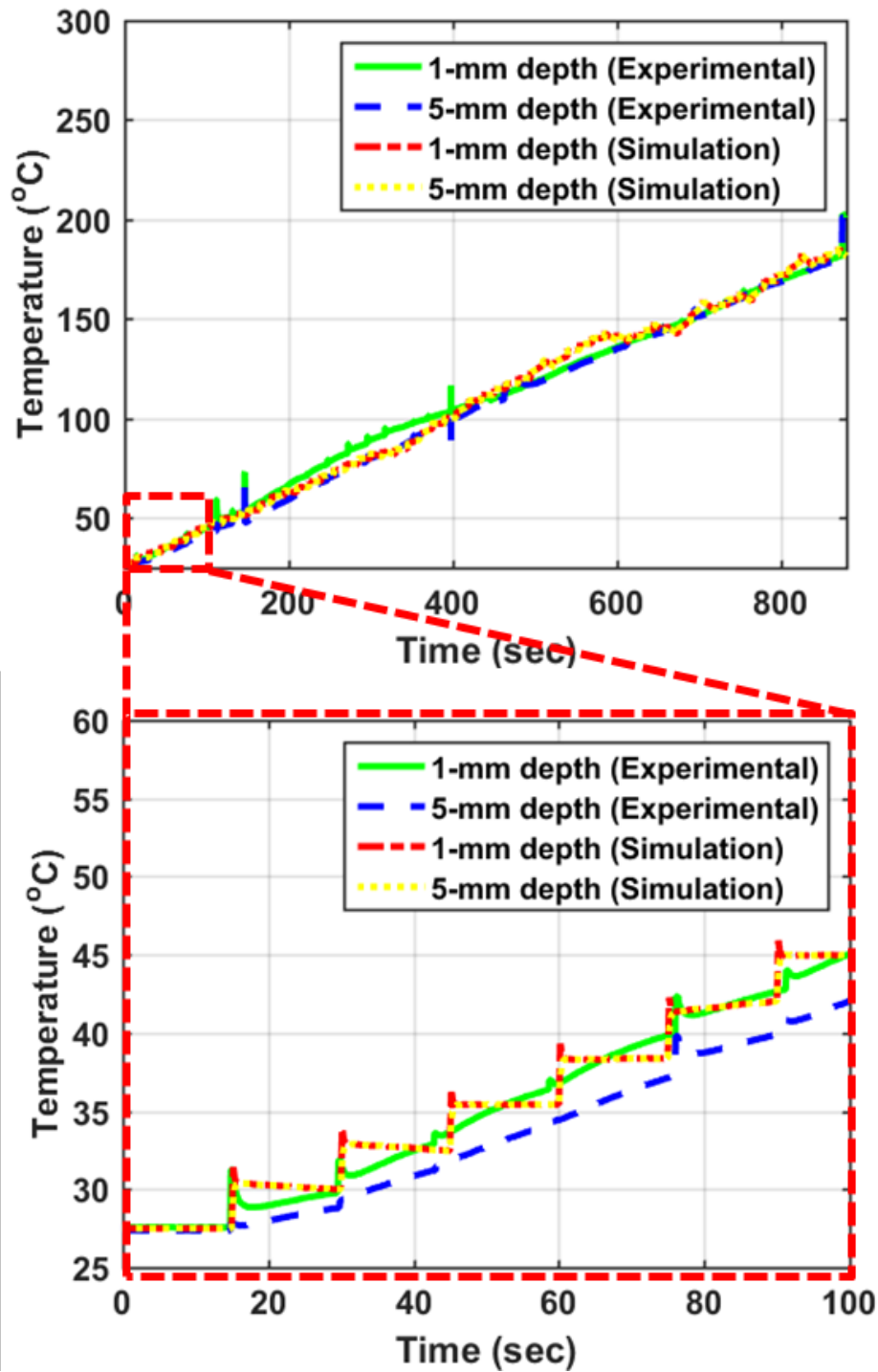


Figure 3-8. Temperature profile at 1-, 5-mm depth of AZ31 sample during LPEB process.

According to the Figure 3-8, the simulation result is well corresponding with the experimental result. However, the thermocouple sensors were not as fast as catch with the temperature profile of LPEB process. It is assumed to be the Mg-alloy has large temperature diffusivity rather than the thermocouple. The principle of the LPEB process is basically identical to the general heat treatment; rapid quenching and tempering. Through the electron transmission and vibration in the surface, the temperature is increased at the melting point for a micro seconds. Then, during the rest time (10 - 20 s), the temperature is abruptly decreased at an ordinary state by a heat diffusion. It can be shown that Figure 3-8, it is increased about 3°C per one LPEB pulse by 10 J/cm² energy density and the temperature at 1-mm and 5-mm depth reaches almost 220°C known as vacancy migration point of Mg-alloys. Above 220°C, its solute-solution distribution phenomenon with surface alloying can modify the microstructure [55]; Mg as the solution and Al as the solute. When the LPEB irradiation is more than 20 cycles (one cycle is 2 by 2 pattern), the temperature is periodically changed in 250 - 300°C. The reason of limitation is anticipated by a high temperature gradient formation and the activated radiation as self-chilling effects on the surface.

3.3.2. Mechanical characteristics analysis

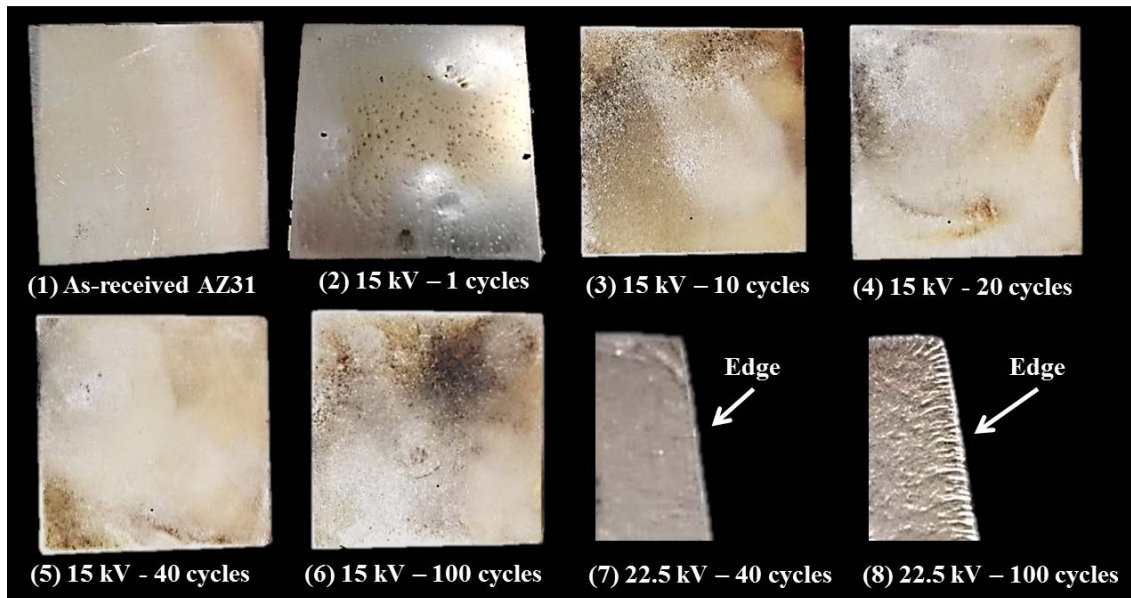


Figure 3-9. Surface images of AZ31 samples at different number of cycles.

Figure 3-9 shows the photograph images of the surface of AZ31 samples when 15 kV and 22.5 kV accelerating voltages are used in LPEB process, which the color and brightness were different with the number of cycles (1, 10, 20, 40, and 100 cycles). The reason of using 15 kV firstly, this accelerating voltage is corresponding to 3 J/cm^2 ; Hao & Li [5], Bo et al [36] and Gao et al [10] has been documented that the 3 J/cm^2 is only used for the HCPEB surface treatment on Mg-alloys. Although the tool mark at the bare surface is removed in the all samples, the surfaces of 1 and 10 cycles were worse than the initial state. Nonetheless, at the 20, 40 cycles shows more brightness surface, but at the 100 cycles, the color of the small part is changed to be blacked. So, it was verified that the surface of the Mg-alloys cannot completely modified to new surface layer when the unsatisfied number of cycles is applied for LPEB process, and vice versa. And the edge deformation is significantly appeared in 22.5 kV samples. Especially, in 100 cycle case, some cracks are detected at the edge. The crack is considered to be critical mechanical defects caused from tensile stress induced by higher brittleness. To sustain the sharp edge of the workpiece, the number of cycles is preferred to not so much. As a result, the 20 and 40 cycles are selected to the interested value of the number of cycles.

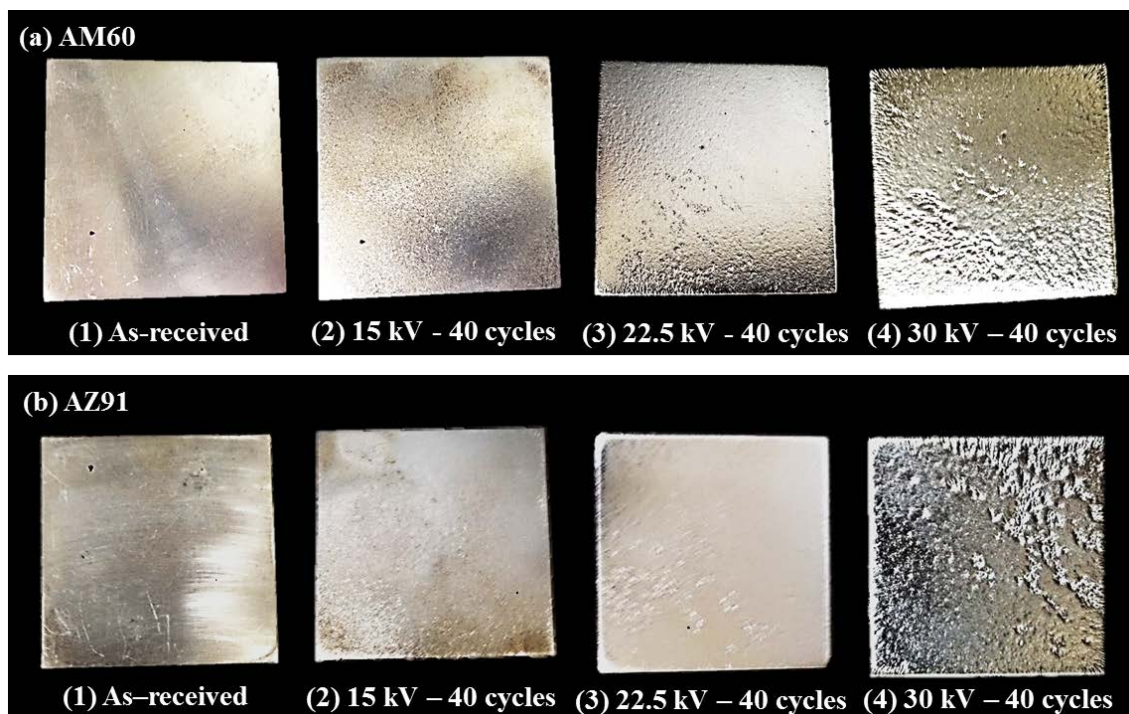


Figure 3-10. Surface images of (a) AM60 and (b) AZ91 at different accelerating voltage.

Then, Figure 3-10 presents the photograph images of the surface of AM60, AZ91 samples when the accelerating voltage is changed from 15 to 30 kV with the number of cycles is 40. At the 15 kV case, the surface is shown to be not bright rather than 22.5, 30 kV cases. Also, the difference with AM60 and AZ91 is not large up to 22.5 kV even though they have different Al content. However, when the accelerating voltage is 30 kV, it was appeared that it is possible to generate the β -precipitation on the AZ91 surface [55]. In addition to, the surface roughness of 30 kV cases seem to be slightly excessive for applying at the engineering application due to the lots of craters. From now on, it is supposed that the accelerating voltage of LPEB is represented by the energy density parameter such that the each 15, 22.5, 27, and 30 kV is equal to 3, 5, 7 and 10 J/cm².

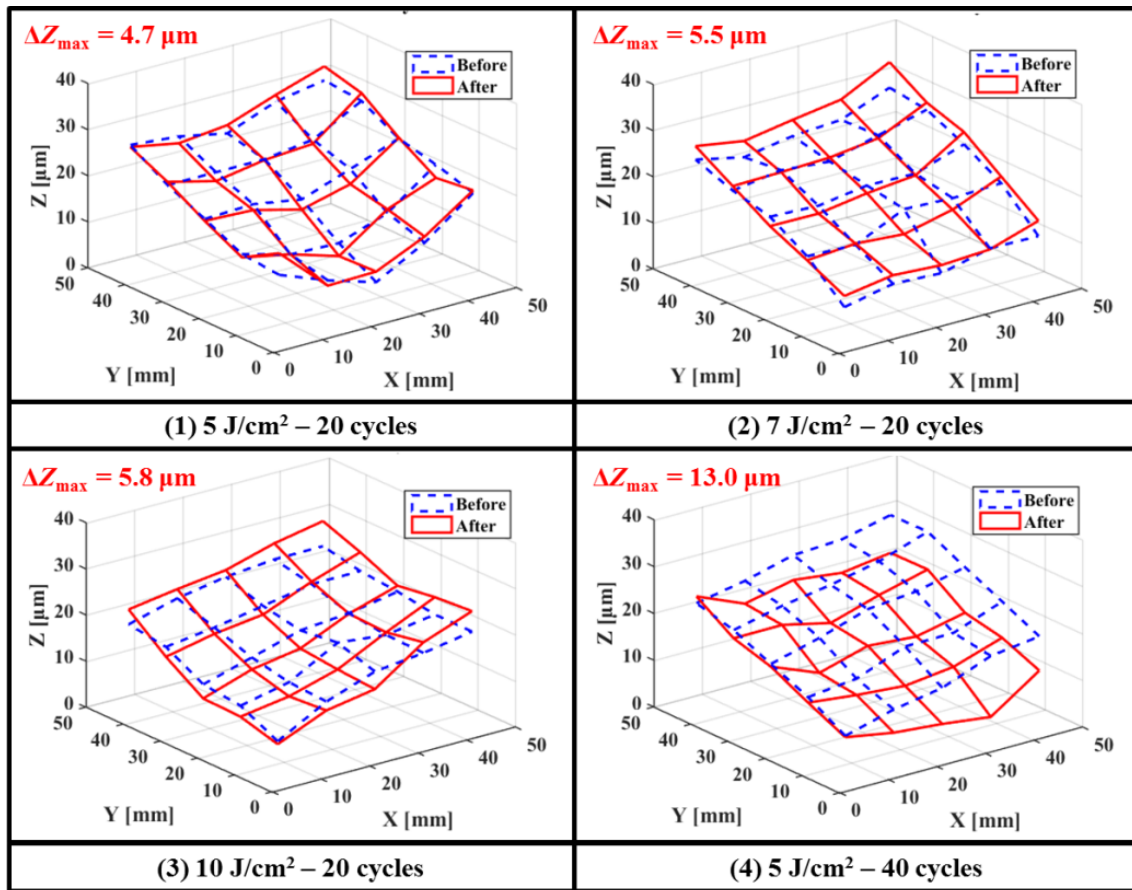


Figure 3-11. Deformation of AZ31 samples in height direction.

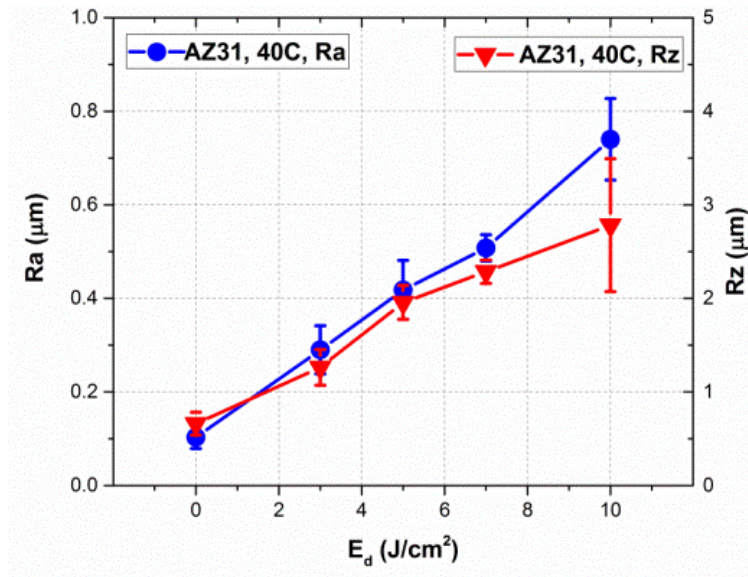


Figure 3-12. 1D surface roughness of AZ31 samples with different energy density.

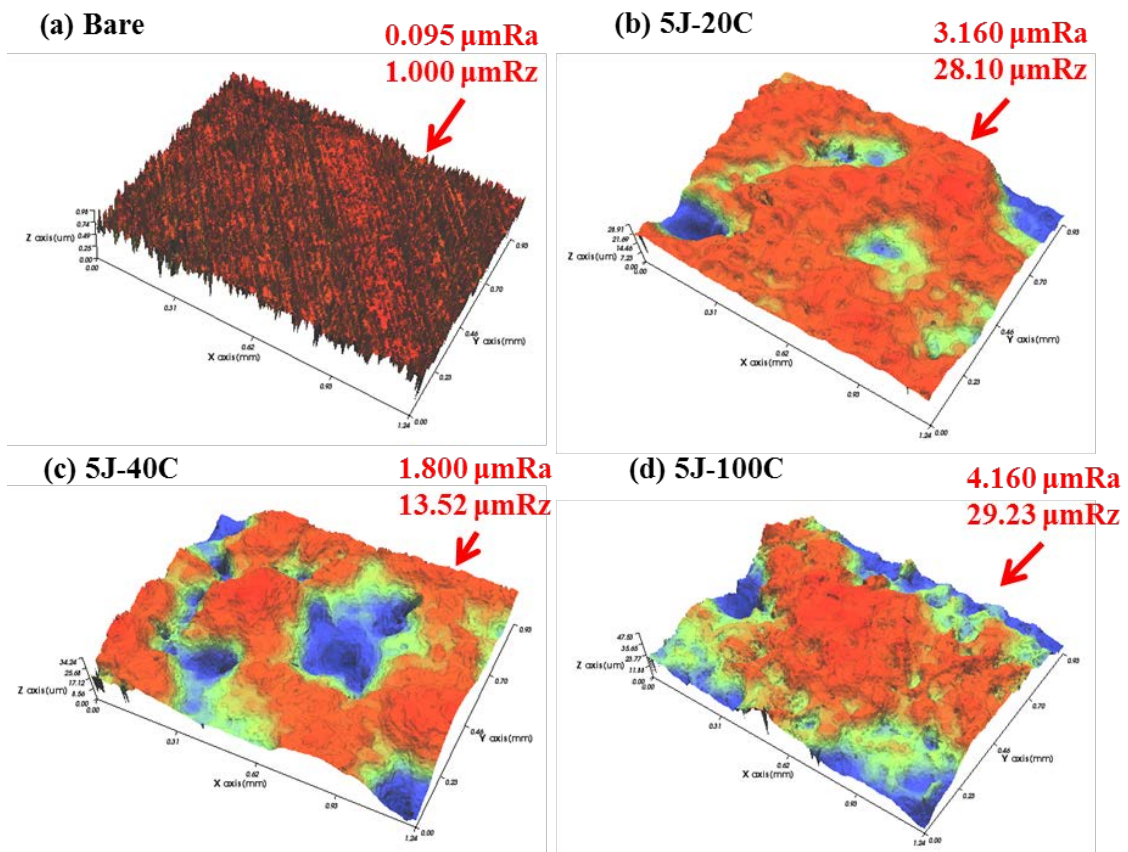


Figure 3-13. 3D surface profile of AZ31 samples with the surface roughness.

At the Figure 3-11, the deformation of z-depth is measured at 4 by 4 points using 'Coordinate Measuring Machine' before/after LPEB process on AZ31 samples. The deformation was measured to $\sim 5 \mu\text{m}$ at 20 cycles with the all energy density cases. Considering the measurement error originated by the reference location changed at each experiments, It was apparently observed that the maximum deformation (ΔZ_{max}) is relatively increased by the growth of the energy density. Especially, the number of cycles is seem to have huge effect on the deformation results of the LPEB process by comparing with the cases of '5 J/cm² - 20 cycles' ($\Delta Z_{\text{max}} = 4.7 \mu\text{m}$) and '5 J/cm² - 40 cycles' ($\Delta Z_{\text{max}} = 13.0 \mu\text{m}$).

Figure 3-12 presents the 1D surface roughness of AZ31 samples according to each energy density cases with 40 cycles. The measurement is enabled by 'Semi Auto Formtracer System'. The results are appeared to be less than 1 μmRa , but there are noticeable tendency such that the Ra and Rz value is increased at higher energy density condition. Hence, in order to control the quality of the surface roughness adequately, 3 - 7 J/cm² range is preferred to Mg-alloys in LPEB process.

Then, referring the Figure 3-12, which was measured by 3D formtracer, the surface roughness is transformed to be harsher by more number of cycles. At '5 J/cm² - 40 cycles' (1.800 μmRa), it shows appropriate performance rather than '5 J/cm² - 100 cycles' (4.160 μmRa). Generally, 0.8 - 1.6 μmRa is recommended in engineering application. Therefore, it is required to adequate number of cycles (less than 40 cycles) for LPEB process of AZ31 Mg-alloy. To sum up with the surface results such as color, brightness, roughness and deformation of LPEB treated sample, the optimum values of energy density and number of cycles are close on 3 - 7 J/cm² and 20 - 40 cycles.

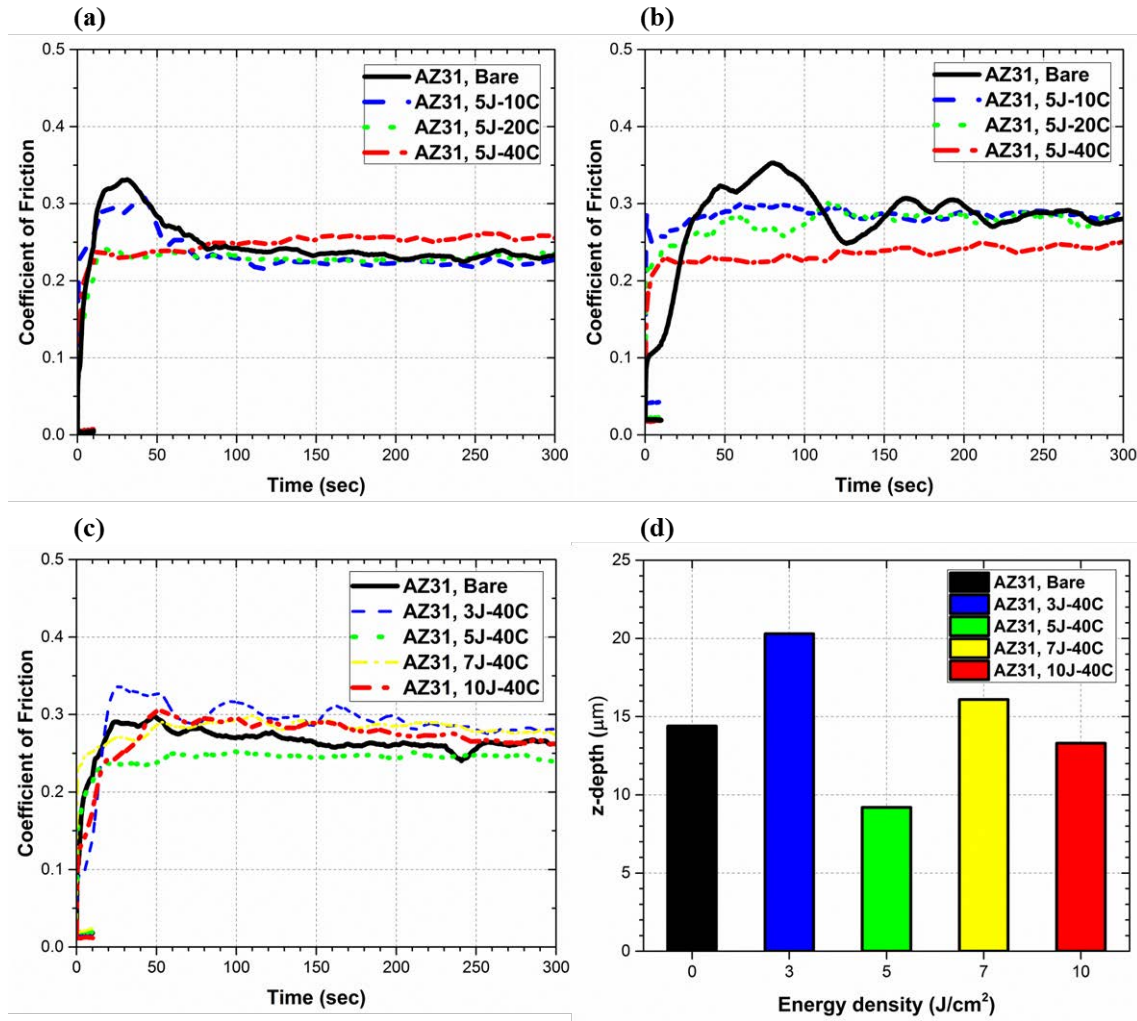


Figure 3-14. COF profile of the Ball-on-disc wear test (a) ' $N = 10\text{ N}$, $V_d = 260\text{ mm/s}$ ($\omega = 500\text{ rpm}$, $r_B = 5\text{ mm}$)', (b) ' $N = 20\text{ N}$, $V_d = 1\text{ mm/s}$ ($\omega = 2\text{ rpm}$, $r_B = 5\text{ mm}$)', (c) ' $N = 20\text{ N}$, $V_d = 105\text{ mm/s}$ ($\omega = 200\text{ rpm}$, $r_B = 5\text{ mm}$)', and (d) maximum wear scar depth of the test (c).

In ball-on-disc wear test when ' $N = 10 \text{ N}$, $V_d = 260 \text{ mm/s}$ ' (Figure 3-14 (a)), the coefficient of friction (COP) of LPEB treated AZ31 surface was decreased from 10 to 50 seconds. From Figure 3-14 (a), the COP of 20 and 40 cycles was recorded at maximum 0.24 while the bare surface was recorded at maximum 0.34. Also, it can be shown that the cases of 20 and 40 cycles were apparently more improved than the case of 10 cycles which was recorded at maximum 0.30. However, after 50 sec, the COP was abruptly changed. The COP of the bare surface and the cases of 10 and 20 cycles were converged at around 0.23, but the COP of the 40 cycles was converged at around 0.25. Considering the amount of LPEB treated AZ31 layer removed by the contacted steel ball during the tests, the COP results when after 50 sec would be regarded as the original material's mechanical properties. So, it could be assumed that the COP results are affected by the total scratched distance of the sample surface.

Compared to the COP results of the ball-on-disc test when ' $N = 10 \text{ N}$, $V_d = 260 \text{ mm/s}$ ', when ' $N = 20 \text{ N}$, $V_d = 1 \text{ mm/s}$ ' (Figure 3-14 (b)) shows different aspect by changing normal force and the speed of the contacted ball. In this test, the COP of LPEB treated AZ31 surface showed more stable than the bare surface from 50 to 150 sec. Following the Figure 3-14 (b), the COP of the 40 cycles was recorded at 0.23 - 0.25, the 10 and 20 cycles were recorded at 0.25 - 0.30, and the bare surface was recorded at 0.25 - 0.35. After 150 sec, the trend was continued, so it was assumed that the different results of COP were affected by the higher normal force of its ball-on-disc wear test. When ' $N = 20 \text{ N}$, $V_d = 105 \text{ mm/s}$ ' (Figure 3-14 (c)), the COP of 3, 7 and 10 J/cm^2 cases are increased than the bare surface. In this test, the trend is kept to the end. Therefore, the insufficient or excessive energy can give the worse surface quality in the view of mechanical characteristics. In addition to, Figure 3-14 (d) represents that the 5 J/cm^2 is the best LPEB condition as showing smallest depth of wear track. To sum up with the all results of three ball-on-disc wear tests, comparing the COP of the bare AZ31 surface, the mechanical properties are apparently improved by LPEB irradiation and the '5 J/cm^2 - 40 cycles' LPEB treated AZ31 surface is observed for the most superior case than the other. It implies LPEB irradiation repeated as many fabricates more distributed molten layer by a re-melting process. Then, its optimum energy density can create a new hardened surface on AZ31 by appropriate surface alloying.

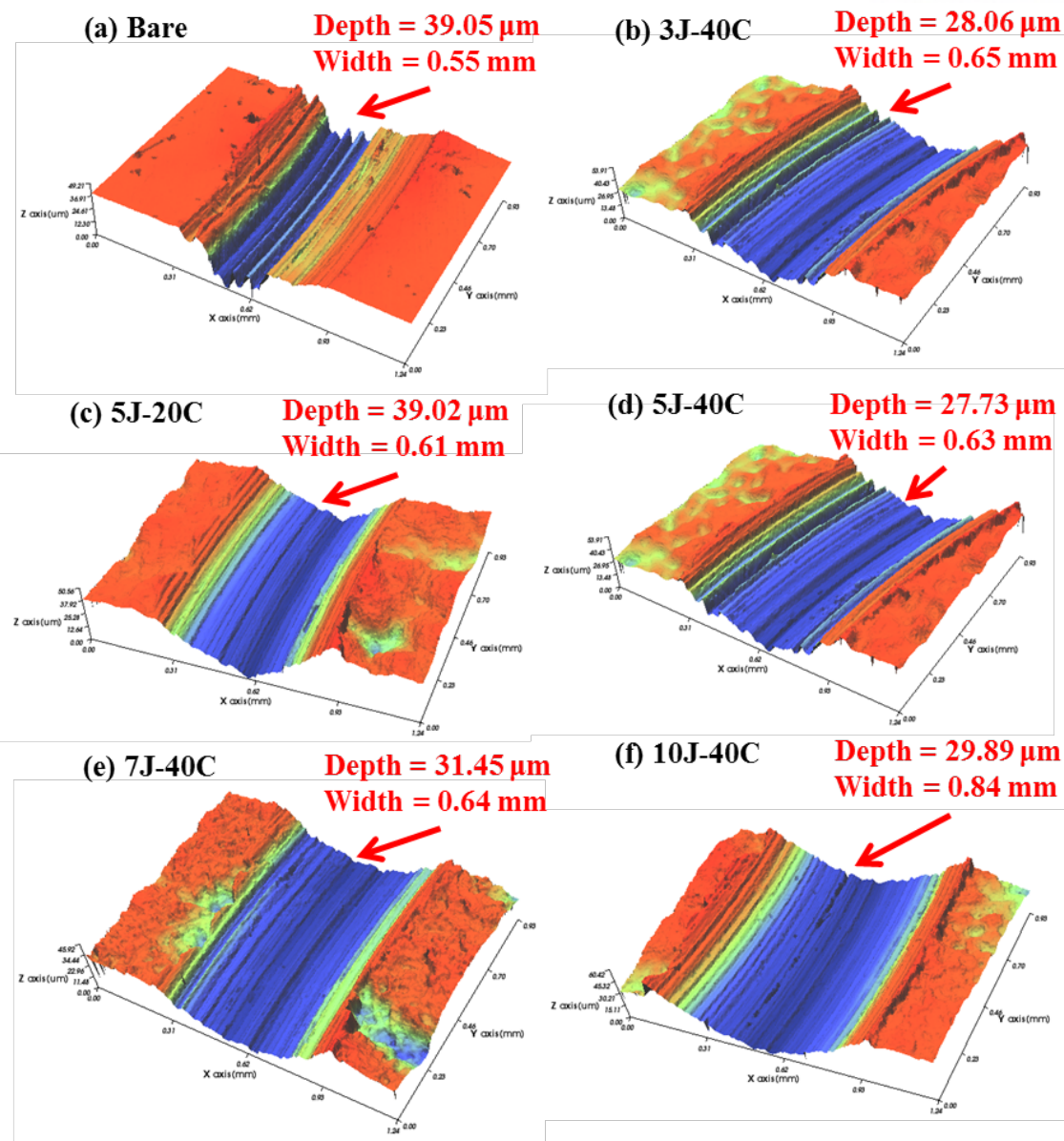


Figure 3-15. 3D surface profile at wear scar of AZ31 samples in ' $N = 20 \text{ N}$, $V_d = 105 \text{ mm/s}$ '.

Figure 3-15 represents the wear scar profile in LPEB treated AZ31 samples. According to those results, ' $5 \text{ J/cm}^2 - 40 \text{ cycles}$ ' condition also shows the best performance among them by appearing the lowest wear scar depth ($27.73 \mu\text{m}$) and intermediate width (0.63 mm). This trade-off phenomenon can be explained by abrasive/adhesive wear mechanism. In macroscopic view, at higher surface roughness, the wear resistance is more degraded because abrasive wear can mainly affect to the mechanical contact between the ball and the surface. On the other hand, in microscopic view, the atomic attraction becomes more significant. Therefore, at lower surface roughness, the wear resistance is more degraded.

3.3.3. Electrochemical characteristics analysis

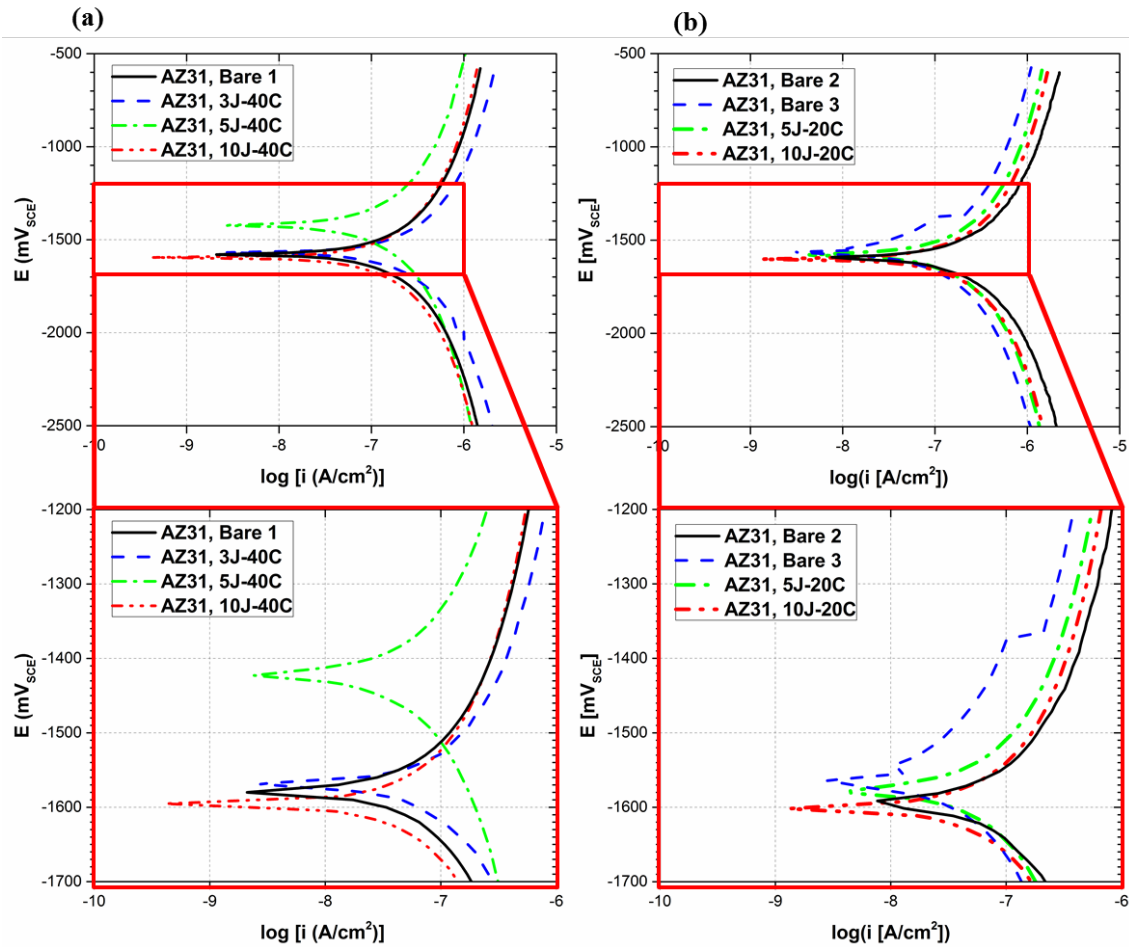


Figure 3-16. Evans-Hoar diagram of AZ31 samples: (a) 40 cycles, (b) 20 cycles.

The electrochemical properties are obtained by experiment of the 3-electrode cell test. First of all, Figure 3-16 provides that the corrosion potential (E_{corr}) and the corrosion current density (i_{corr}) based on the results of the potentiodynamic polarization. E_{corr} is preferred as high because the ionization tendency of the material is lessened with high open circuit potential ($\text{OCP} = E_{\text{corr}}$). Conversely, i_{corr} is preferred to low because it determines the rate of ionization. According to the Figure 3-16 (a), E_{corr} of the ‘Bare 1’ AZ31 sample is $-1579 \text{ mV}_{\text{SCE}}$, and the LPEB treated AZ31 sample applied ‘ $5 \text{ J/cm}^2 - 40$ cycles’ is improved to $-1421 \text{ mV}_{\text{SCE}}$. The potential difference is $158 \text{ mV}_{\text{SCE}}$; it indicates some positive changes were occurred in that surface such as modifications of the chemical composition and the grain structure. However, the corrosion properties were not improved by ‘ $3 \text{ J/cm}^2 - 40$ cycles’. Although the E_{corr} was slightly ascended, the i_{corr} was negatively changed. Generally, the i_{corr} is more significant to evaluate the corrosion resistance. Figure 3-16 (b) indicates that 20 cycles are insufficient

to improvement of the electrochemical properties. Also, the results of ‘Bare 2’ and ‘Bare 3’ shows different aspect of polarization curve. It is expected that it was caused from the locally different surface state.

The results of the corrosion properties can be expressed quantitatively at Table 3-3. At ‘5 J/cm² - 20 cycles’, the corrosion rate ($v_{\text{corr}} = 3.50 \times 10^{-4}$) was the slowest. Comparing to the ‘Bare 3’ ($v_{\text{corr}} = 4.91 \times 10^{-4}$), it was reduced by 29%. Then, the Tafel slopes (β_a, β_c) represent the modeling parameter for estimating R_p using Eq. (3.15). Among the LPEB treated samples, the R_p of ‘5 J/cm² - 40 cycles’ was the most superior to the other parameter. The R_p of ‘3 J/cm² - 40 cycles’ was calculated by 461.6 k Ω ·cm². At the LPEB treated sample of ‘5 J/cm² - 40 cycles’ was estimated to 882 k Ω ·cm². It is observed that the 91% improvement of corrosion resistance at the optimum energy density parameter. The number of cycles was not significant in the polarization tests. On the other hand, the R_p of and ‘Bare 3’ is larger than the LPEB treated sample. The R_p of ‘Bare 3’ was estimated to 905 k Ω ·cm². The each bare surface sample shows abnormally large difference at changed their measurement location. Its unstable characteristic changes are also observed in the polarization curves. In Figure 3-16 (b), the plot of ‘Bare 3’ was abruptly curved in the between -1400 to -1300 mV_{SCE}. The unstable curve indicates the presence of the frail oxide layer.

Table 3-3. Corrosion analysis results obtained by linear polarization method.

AZ31	E_{corr} (mV _{SCE})	i_{corr} (mA/cm ²)	v_{corr} (mm/year)	β_a	β_c	R_p (k Ω ·cm ²)
Bare 1	-1579	3.30×10^{-5}	7.23×10^{-4}	0.248	0.225	658.4
Bare 2	-1595	4.35×10^{-5}	9.54×10^{-4}	0.253	0.204	490.3
Bare 3	-1559	4.59×10^{-5}	10.1×10^{-4}	0.515	0.383	905.0
3J-40C	-1570	4.71×10^{-5}	10.3×10^{-4}	0.208	0.263	461.6
5J-40C	-1421	2.46×10^{-5}	5.40×10^{-4}	0.192	0.275	882.8
5J-20C	-1576	1.60×10^{-5}	3.50×10^{-4}	0.126	0.127	748.3
10J-40C	-1596	2.96×10^{-5}	6.49×10^{-4}	0.239	0.235	735.1
10J-20C	-1601	3.76×10^{-5}	8.25×10^{-4}	0.241	0.226	625.8

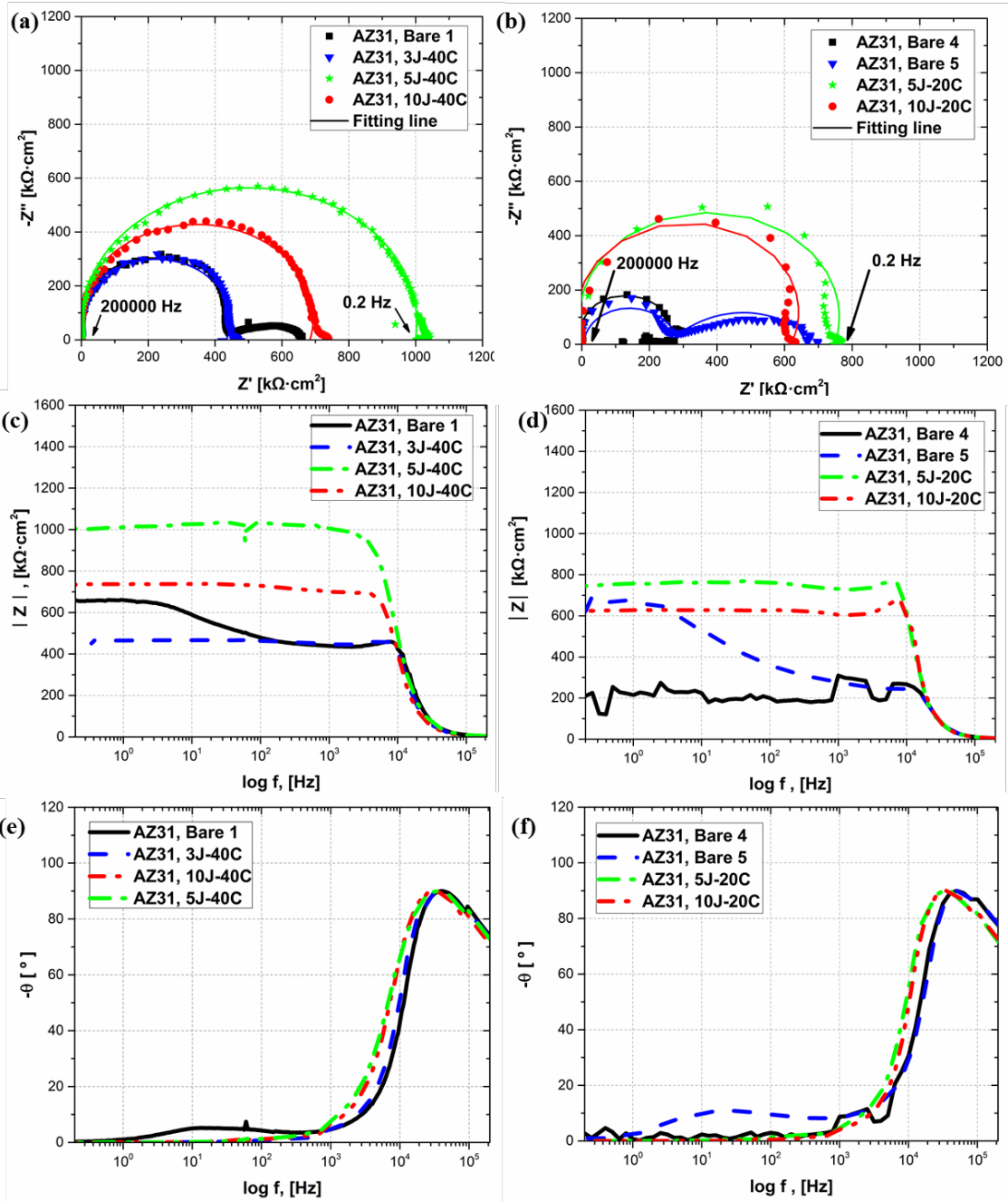


Figure 3-17. (a), (b) Nyquist plot, (c), (d) Bode magnitude plot, and (e), (f) Bode phase plot of AZ31.

Figure 3-17 shows the results of electrochemical impedance spectroscopy. At Figure 3-17 (a), the curve of the ‘Bare 1’ is plotted by the double circle shape. The circle at low frequency seems to represent the oxide layer of the AZ31. Therefore, it can be assumed that the circle at high frequency represents the original impedance of the bare surface. It is supported by Figure 3-17 (b), the ‘Bare 4’ shows only single circle without additional impedance elements different from ‘Bare 5’. Referring to Figure 3-17 (c), (d), it can be checked the impedance changes versus frequency. At 10 - 100 Hz, it is observed that the magnitude of ‘Bare 1’, ‘Bare 5’ was decreased. Especially, at Figure 3-17 (d), the ‘Bare 4’ shows unstable curves at low frequency rather than the other LPEB treated sample. It implies the LPEB process fabricates more stable surface layer by re-melting process substituting the oxide layer. Generally, this instability was occurred at the sample presented by single circle in Nyquist plot. Thus, Figure 3-17 (d) indicates that if some mechanical abruption is occurred such as scratching and pitting, the corrosion resistance can be critically reduced by the oxide layer is removed. To sum up the results of the AZ31 bare surfaces, it was verified the additional requirement for fabricating a corrosion-protection layers on AZ31 although it has been recognized the function of the oxide film is very important.

Table 3-4. Fitting results of equivalent circuit modelling for EIS curve.

AZ31	R_s ($k\Omega \cdot cm^2$)	Q_f (nF)	n_f	R_f ($k\Omega \cdot cm^2$)	Q_{dl} (nF)	n_{dl}	R_{ct} ($k\Omega \cdot cm^2$)
Bare 1	10.90	166.7	0.517	249.8	0.000151	1.24	411.7
Bare 4	5.704	-	-	-	0.334	1.23	249.8
Bare 5	6.430	0.001214	0.642	419.2	0.00850	0.998	263.9
3J-40C	10.04	-	-	-	0.00578	1.22	423.9
5J-40C	4.160	-	-	-	0.00480	1.08	995.1
5J-20C	7.037	-	-	-	0.0307	1.17	741.0
10J-40C	8.214	-	-	-	0.00513	1.16	675.7
10J-20C	11.43	-	-	-	0.0269	1.24	607.2

At Table 3-4, the modelling parameters used in this simulation are provided. The R_s was estimated to 4 - 12 $\text{k}\Omega\cdot\text{cm}^2$, in the tests. Since the value of R_s is relatively small, the state change of NaCl solution can be dismissed. If the system has film elements, the Q_f and n_f were obtained with R_f . The R_f was significant compared to R_{ct} , but the value of charge phase elements showed no special feature. The best LPEB parameter was determined by evaluating the R_{ct} . The R_{ct} was crucially affected by the energy density. Although the LPEB process did not show good performance when applying 3 and 10 J/cm^2 , the R_{ct} was improved relatively large by 5 J/cm^2 . To compare with '3 J/cm^2 - 40 cycles' (423.9 $\text{k}\Omega\cdot\text{cm}^2$) and '5 J/cm^2 - 40 cycles' (995.1 $\text{k}\Omega\cdot\text{cm}^2$), it was increased by 135%. The number of cycles did not induce a major modification, but there are some tendencies such that the more LPEB cycles were irradiated, the more increment of R_{ct} was appeared. Then, the R_{ct} of the 'Bare 1' was estimated to 411.7 $\text{k}\Omega\cdot\text{cm}^2$. Therefore the bare surface was increased by 142% after LPEB process. However, in order to evaluate the corrosion resistance at the original surface, the oxide film resistance (R_f) is also to be concluded. Therefore, considering the total corrosion resistance of 'Bare 1' ($R_{\text{corr}} = R_{ct} + R_f = 661.5 \text{ k}\Omega\cdot\text{cm}^2$) and 'Bare 5' ($R_{\text{corr}} = R_{ct} + R_f = 683.1 \text{ k}\Omega\cdot\text{cm}^2$), it showed an improvement of 45% - 50%.

3.4. Summary

In this chapter, LPEB surface treatment on AZ31 is simulated using prediction model and investigated by mechanical and electrochemical analysis. The energy absorption profile of the depth and the lateral is approximated using Gaussian distribution, which is affected by the atomic number and the accelerating voltage. The prediction model helps for selecting the optimum parameters of the LPEB process on AZ31 (irradiation pattern, energy density, and number of cycles). The pitch of the irradiation pattern is established to 20 mm by energy absorption model and the accelerating voltage candidates are shorted to 15 - 30 kV. Then, the FDM simulation is reasonably matched with the results of temperature measurement. The temperature of AZ31 is reached at 220°C when over 20 cycles which enables the eutectic reaction of Mg and Al.

In mechanical characteristics analysis, the surface roughness and color with brightness are presented. As a result, it was proved that the surface of Mg-alloy is easily evaporated by LPEB and the new more brightness surface layer is fabricated when energy density is over 3 J/cm^2 . Also, the deformation diagram and ball-on-disc wear test is used for parameter optimization of LPEB process. In the coefficient of friction analysis, the large number of cycles is preferred to withstand the wear even though the deformation is increased. And, at 5 J/cm^2 cases, the surface hardening was magnified.

In electrochemical characteristics analysis, the corrosion resistance of each AZ31 sample is

evaluated by the potentiodynamic polarization test and EIS in 3.5 wt.% NaCl solution. Although, at some cases, the corrosion resistance of the bare surface is larger than the LPEB treated surface due to the oxide layer, it was very unstable. Finally, '5 J/cm² - 40 cycles' condition showed the best performance for protecting the corrosion as well as the mechanical contact.

IV. Metallurgical investigations on the surface of large pulsed electron beam treated Mg-alloys

4.1. Introduction

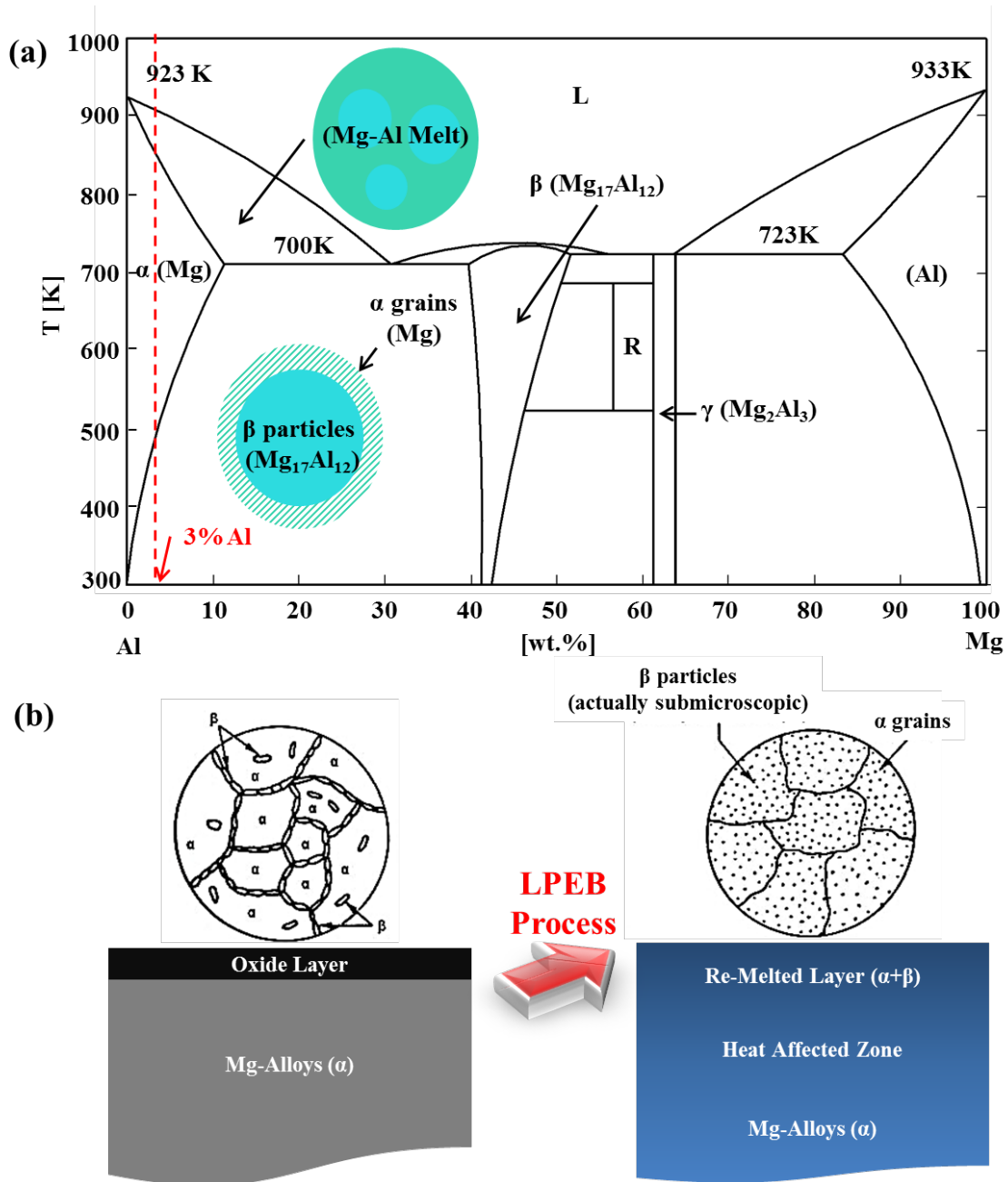


Figure 4-1. (a) Phase diagram of Mg-Al system and (b) schematics of LPEB surface modification onto Mg-alloys.

Figure 4-1 (a) shows the phase diagram of Mg-Al alloy system. It is easily dissolved by eutectic reaction and melted at the higher temperature with higher Al content. However, since the evaporation point of the Mg (1091 °C) is relatively lower than the other metal, especially such as Al (2470 °C), the high energy density of LPEB parameter is possible to cause unfavorable surface quality in inhomogeneous Mg-alloys. The principle of the modification on LPEB treated surface is shown at Figure 4-1 (b). Simultaneously the oxide layer is removed by LPEB, the new nano-grained metastable gradient layer formed by LPEB, which is can be divided into re-melted layer, heat affected zone, and the original grain structure. The number of cycles of the LPEB parameter is also well controlled to satisfy the stable qualities because the effects of the LPEB surface modification is due to the repeated re-melting process with rapid self-quenching.

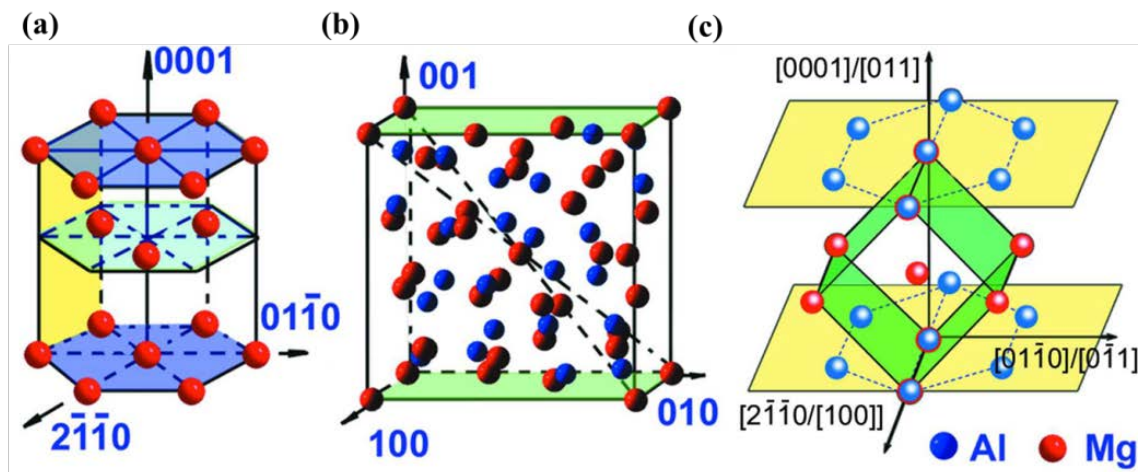


Figure 4-2. The crystal structures of the two phases in the transformation system α -Mg/ β -Mg₁₇Al₁₂: (a) hcp α -Mg, (b) bcc β -Mg₁₇Al₁₂ and (c) schematic diagram between hcp and bcc structures (Liu et al. [56]).

Figure 4-2 presents the mode of crystal structures of Mg-Al lattice. The microstructure is transformed to new re-crystallized layer has more dense and well distributed β particles in α grains. Even though the α -phase has denser hcp structure, the β -phase has more complicated relationship between Mg and Al. Therefore the β structure is preferred to withstand the wear/corrosion attacks. On the other hand, the problem of brittle failure, such as delamination, can be generated at over enriched β structure film coated by surface treatment (PEO, DLC, LSM, and etc.). For these reason, it is important to sustain the ductile property of the original Mg-alloys. It is expected that the gradient layer fabricated by LPEB process is performed to such intermediate roles between the brittle coated film and the ductile original substrate.

For metallurgical analysis, the micron level images and chemical composition data are required. The SEM & EDS analysis were implemented to examination, which is performed by ‘Nano Nova SEM (model: Nano 230)’ at UCRF in UNIST. It can be visualization for the morphology of the Mg-alloy’s microstructure by a continuous electron beam scanning. Then, at 20 kV accelerating voltage condition, the EDS analysis was executed. The EDS identifies the chemical composition of the Mg-alloy sample. It can evaluate the Al content in LPEB treated surface.

4.2. Microstructure transformation

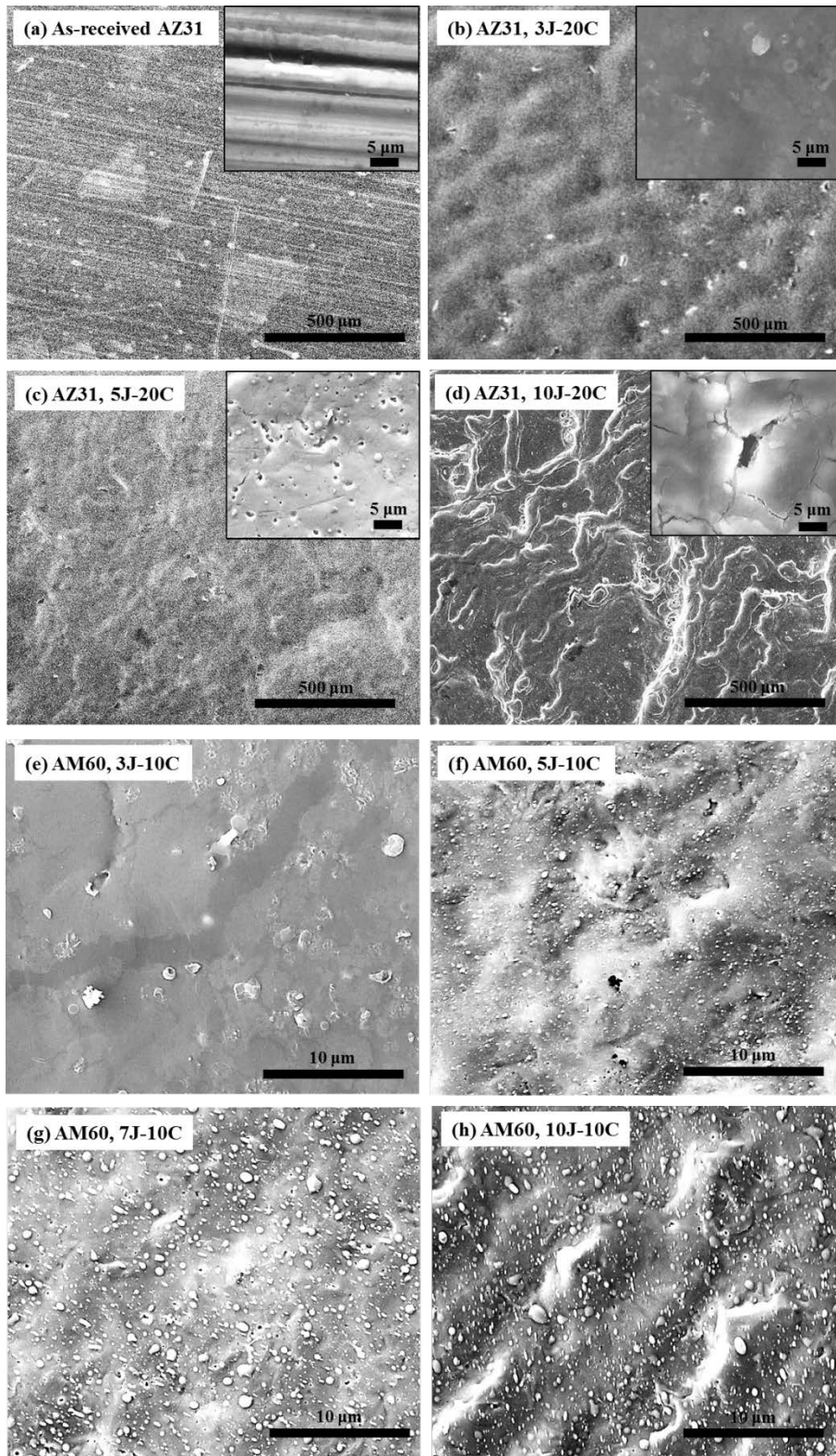


Figure 4-3. SEM image of LPEB treated AZ31 and AM60 at different energy density.

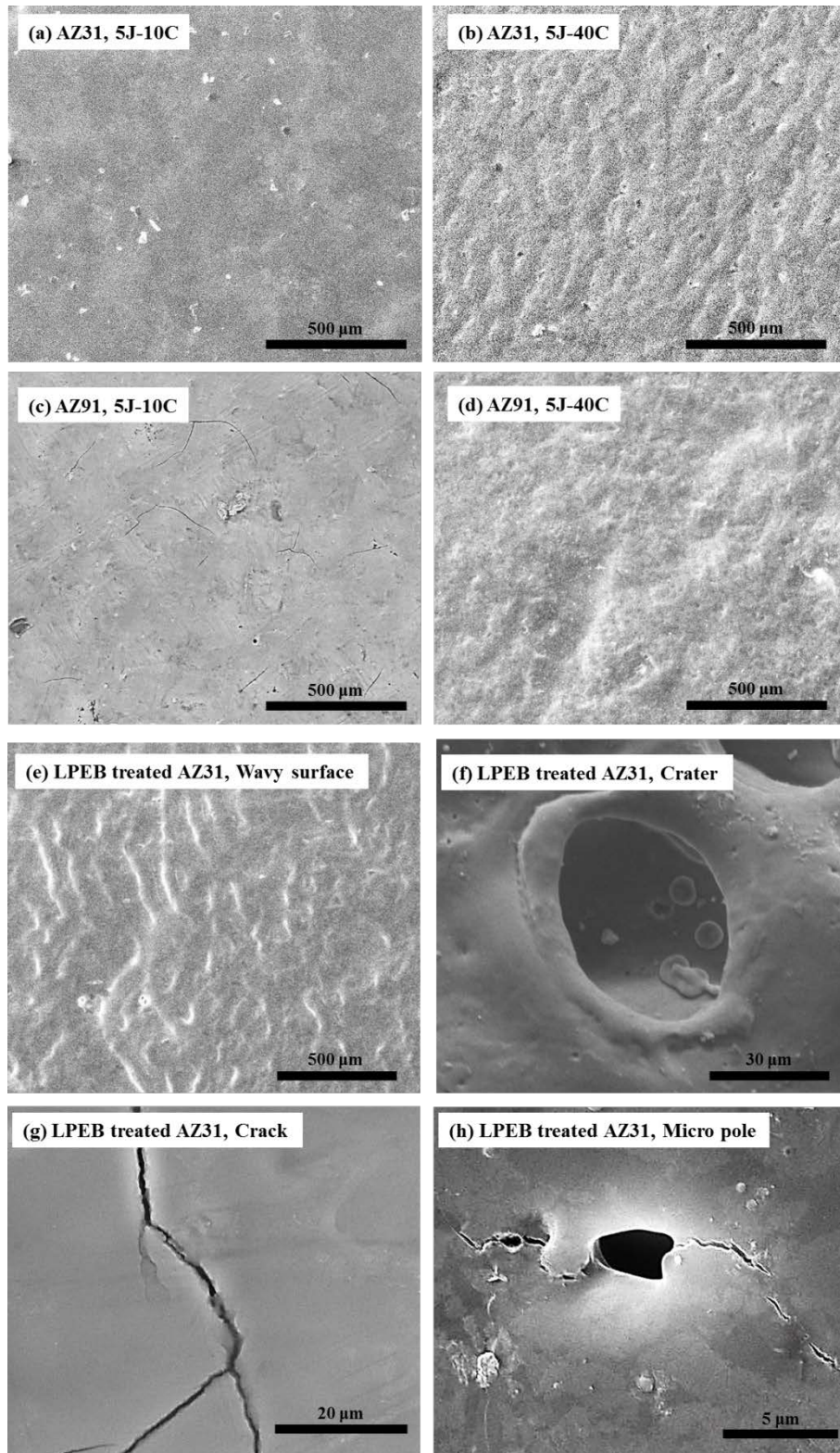


Figure 4-4. SEM image of LPEB treated (a), (b) AZ31, (c), (d) AZ91 and (e) – (h) defects.

Figure 4-3 shows the SEM image of the LPEB treated Mg-alloys as changed by energy density. In Figure 4-3 (a) - (d), it is presented that the results of AZ31. In case of bare surface, the sharpened tool marks are mainly observed. Fundamentally, the general machining/grinding process for Mg-alloys could not remove the micro edges. However, the LPEB treated surface shows completely different surface morphologies. The tool mark is entirely removed in the surface with re-melting process. In addition, the new protruding contours are detected in LPEB treated surface. Then, it seems to the effects of surface modification depends on the beam energy density level. At 3 J/cm^2 , the surface shows the clear morphology in magnified view although it is little curved at large area. At 10 J/cm^2 , it is shown that the surface is transformed to be harsher with many defects. In 5 J/cm^2 , the surface clearness is presented to the medium class but there are some micro poles in magnified view. According to Figure 4-3 (e) - (h) indicates similar results of energy density parameter at AM60. In its more magnified images of AM60 surface, small particles are detected. The size of the particles is increased by higher energy density condition. Evenly, at 10 J/cm^2 , the aggregated mountains of the particles are appeared. It is anticipated that the $\beta\text{-Mg}_{17}\text{Al}_{12}$ particles are actively formed in the LPEB treated surface when high energy density conditions due to the alloying effects.

In Figure 4-4 (a) - (d), the effects of the number of cycles of LPEB are certified. Comparing the 10 cycles and the 40 cycles at same energy density, the more number of cycles shows the more turbulence structure such as wavy surface. At 10 cycles, the surfaces show just plane structure, but, at 40 cycles, it is modified to more grooved shape. The reason is expected to the over repeated dissolved process. However, even though the morphologies of 40 cycles are shown more waved structure, following to the results of chapter 3, the 40 cycles could fabricate better distributed α - β metastable layer than the 10 cycles. Also, that snake-skin-like-surface expects to improve hydrophobic characteristic of Mg-alloys. From Figure 4-4 (e) - (g), the defects of LPEB treated surface are presented. As shown at Figure 4-4 (e), the over wavy surface can be generated by over repeated LPEB cycles. Adequate waviness could improve the corrosion resistance to be high hydrophobic, but it is also could reduce the corrosion resistance because that rough surface is weak at pitting corrosion. Then, at Figure 4-4 (f) - (h), it is demonstrated that the crater, crack and micro pole were frequently detected in micro range at the LPEB treated surface. It is supposed that the defects are produced from the inhomogeneous evaporation by the excessive heat energy applied at Mg-alloys.

To sum up the SEM image analysis, the qualities are largely affected by the energy density and the number of cycles of LPEB process. Especially, the grain boundary, vulnerable to galvanic corrosion, is not detected in LPEB treated surface. Nonetheless, the limitations of LPEB process are confirmed such as crack, micro pole and the particle aggregation. Finally, it is verified that the LPEB process can fabricate the nano-grained α - β stable surface layer on the Mg-alloys

4.3. Chemical composition transformation

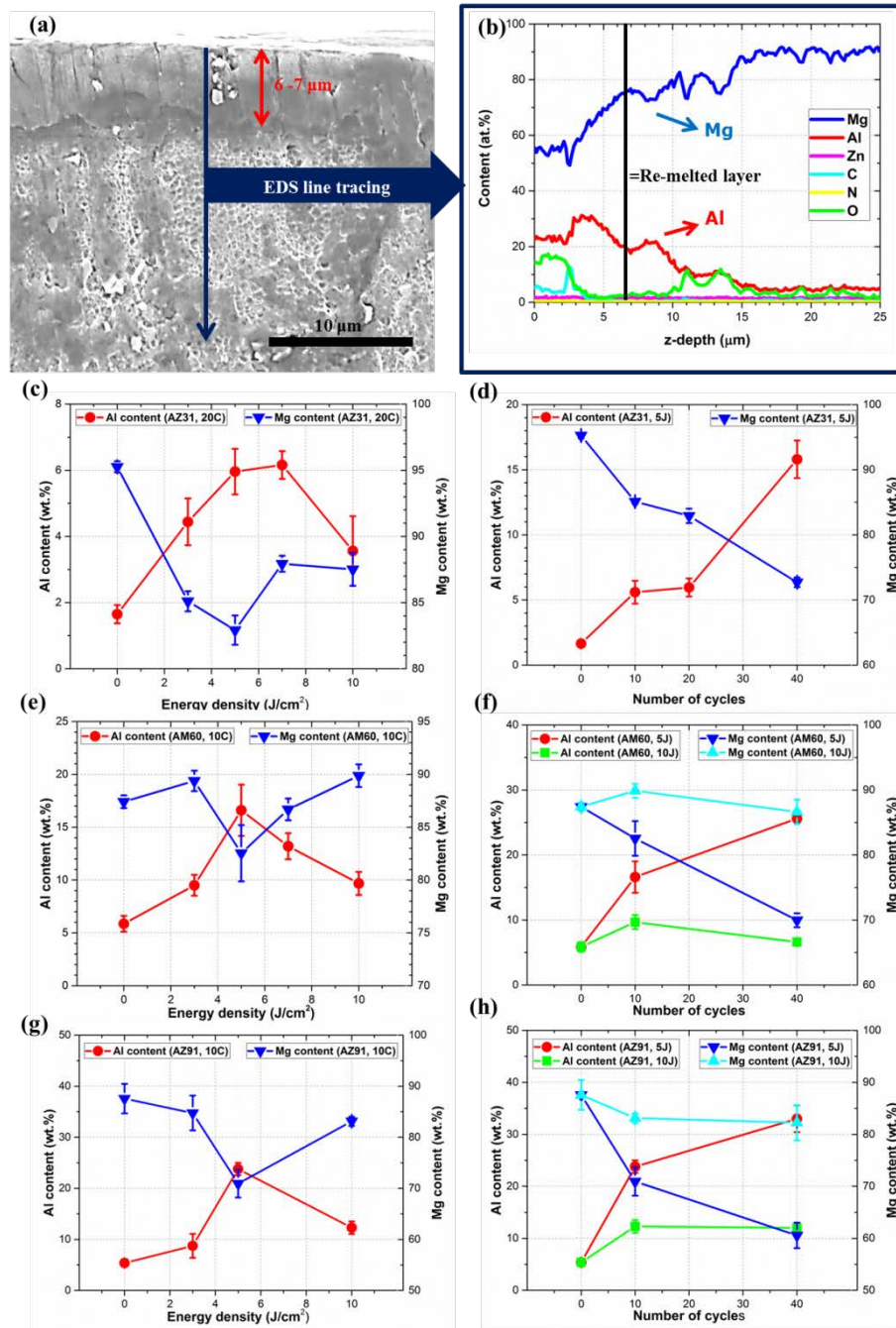


Figure 4-5. (a) Cross-section SEM image of LPEB treated AZ91 (5 J/cm² – 5 cycles), (b) the result of EDS line tracing of (a), and (c) - (h) Al/Mg content profiles of LPEB treated surface of Mg-alloys: (c) AZ31 at the energy density change, (d) AZ31 at the number of cycles change, (e) AM60 at the energy density change, (f) AM60 at the energy density change, (g) AZ91 at the energy density change, and (h) AZ91 at the number of cycles change.

The chemical composition of the Mg-alloys is completely transformed by LPEB process. In Figure 4-5, the grain structure results of the LPEB treated AZ31, AM60, and AZ91 are presented using EDS. According to Figure 4-5 (a), the dense nano-grained structures are appeared at LPEB treated surface. When the energy density was 5 J/cm^2 , the thickness of re-melting surface layer was $6 - 7 \text{ }\mu\text{m}$. It is reasonably verified by LPEB simulation results at Chapter 3. Also, referring Figure 4-5 (b), it was discovered the higher Al contents at the all LPEB treated surface compared to the bare. This special effect can be described to selective evaporation attributed by Al (MP: 660°C , BP: 2470°C) has relatively high boiling point compared to Mg (MP: 650°C , BP: 1091°C). Therefore, there is some optimum range of selective evaporation of Mg in Mg-Al alloy system.

For find the optimum parameter of LPEB process, it was determined that the 'Al/Mg content ratio' is reached at maximum. According to Figure 4-5 (c), (e), and (g), the 5 J/cm^2 was proved the best energy density condition. Between 4 and 6 J/cm^2 , some optimum range for enrich Al content is existed. Then, from Figure 4-5 (d), (f), and (h), the best number of cycles was verified to the 40 cycles case. It is anticipated that LPEB repeated more and more, the gap of Mg and Al content is more amplified. Conversely, the defects are also amplified by large number of cycles according to surface SEM results. Therefore, the optimum parameter of LPEB process can be selected to ' $5 \text{ J/cm}^2 - 40$ cycles' in the view of the chemical composition with minimizing the defects of LPEB process. At Figure 4-5 (d), the Al content of AZ31 sample is increased from 1.65 to $15.8 \text{ wt.}\%$ by LPEB process using ' $5 \text{ J/cm}^2 - 40$ cycles'. Likewise, at Figure 4-5 (f), it is increased from 5.86 to $25.6 \text{ wt.}\%$ and at Figure 4-5 (h), it is increased from 5.38 to $33 \text{ wt.}\%$. The increment of Al content can explain the formation of the new crystalized surface layer.

In conclusion, this EDS results are significantly used to analysis the improvement of the mechanical and electrochemical characteristics because the modified chemical composition results are well-matched with the results of the wear/corrosion tests in Chapter 3. The 5 J/cm^2 parameter is specially designed for the Mg-alloys. Mostly, the higher energy density of LPEB has been performed for surface treatment process. However, since the difference of the evaporation point of the Mg and Al, the optimum energy level is existed for appropriate LPEB process.

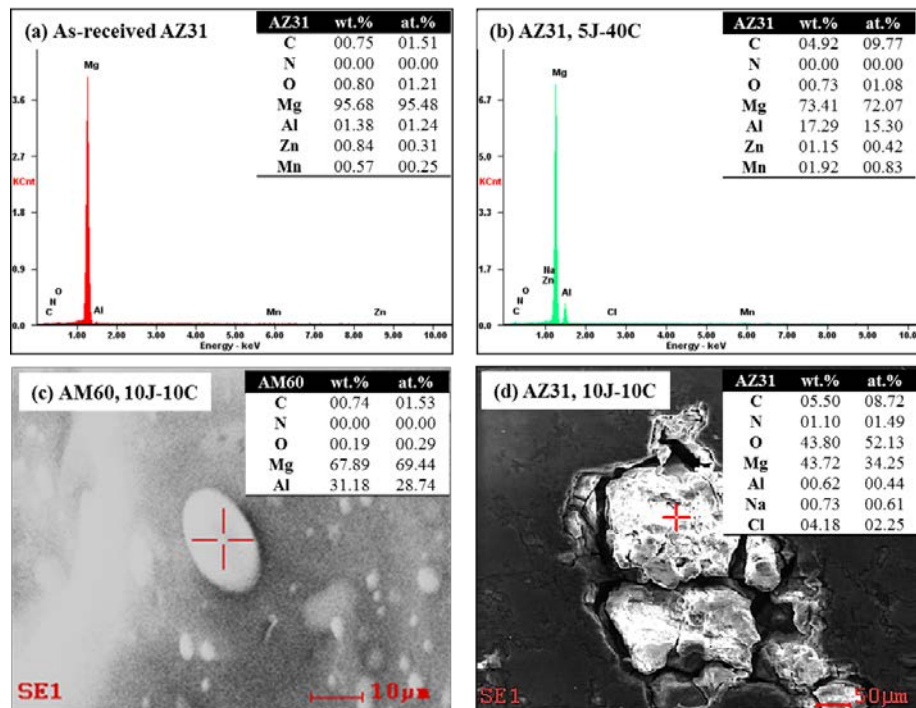


Figure 4-6. EDS results of (a) as-received AZ31, (b) the AZ31 surface treated by the optimum LPEB process (5 J/cm^2 - 40 cycles), (c) the particle in the surface of AM60, and (d) the location of corrosion test of AZ31 sample treated by LPEB process (10 J/cm^2 - 10 cycles).

Finally, Figure 4-6 presents the total chemical composition of the samples. In Figure 4-6 (b), it is appeared some carbon component. Even though it could be generated by dirt in the vacuum chamber, it seems to be more related to other metal component, especially Al because, at the bare of AZ91, the carbon was also detected. Using Figure 4-6 (c), it can be verified the identity of the particles aggregated in LPEB treated AM60 surface presented at Figure 4-4 (h). The Al content of the particle is abnormally high rather than other place. Therefore, it is estimated that the remained $\text{Mg}_{17}\text{Al}_{12}$ components are aggregated not solidified in the Mg grains. Figure 4-6 (d) shows the corrosion product of LPEB treated AZ31. At the fractured position, the large oxide component is detected. It is supposed that the component is attributed to pure Mg in corrosion product is easily reacted with oxygen in atmosphere or OH in water because there are only small Al content with some Na, Cl components. In conclusion, it is demonstrated that it is actually important to fabricate the well distributed and dense Mg-Al alloy system for withstand the galvanic corrosion generated in α - β grain boundary and other unknown attacks. At the ' 5 J/cm^2 - 40 cycles', it is anticipated the recrystallization process is extremely activated than other LPEB conditions.

4.4. Summary

The metallurgical investigations of the LPEB treated Mg-alloys sample were demonstrated in the chapter. Applying the SEM & EDS analysis, the information of the surface morphologies and chemical components was obtained. Then, the limitations of the energy density and number of cycles of LPEB parameter are specified using the qualitative evaluation of the sample surfaces. Also, it was proved that the variable defects are generated by LPEB process such as crack, micro pore and the β -particle aggregation. Then, the EDS result substantiates the optimum parameter of LPEB process. The 'Al/Mg content ratio' is used for finding the optimum parameter and some additional EDS analysis in the whole chemical component modification is accompanied. Finally, the '5 J/cm² - 40 cycles' was selected to the optimum parameter of the LPEB surface treatment for the Mg-alloys.

V. Conclusions and recommendations

5.1 Conclusions

This dissertation presents a technique to improve corrosion resistance of Mg-alloys using LPEB process. Fabrication of a nano-grained Al enriched metastable layer on as-received AZ31 large-area surface with lower power consumption is purpose of LPEB. In previous studies, parameters of pulsed electron beam for Mg-alloys are limited such that irradiation pattern is fixed at only center of workpiece, energy density is 2.5 - 3 J/cm² and optimum number of pulses is 15 [5, 6, 8, 36]. To overcome the previous corrosion improvement performance with parameter optimization, mechanical and electrochemical characteristics analysis and metallurgical verifications are described in each Chapter 3 and Chapter 4. The following conclusions were obtained from this dissertation.

- The optimum irradiation pattern is estimated applying mathematical modelling. The pitch of stitching process is selected less than effective diameter (ϕ_{eff}) 24 mm.
- The electron beam energy absorption profile is modeled using Gaussian distribution. The maximum penetration depth is increased at low atomic number and high accelerating voltage. For Mg-alloys, the accelerating voltage is shorted to 15 - 30 kV.
- In the rest of LPEB pulse, the temperature is increased over eutectic migration point of Mg-alloys (220 °C) at more than 20 cycles with repeated rapid self-quenching effect. The re-melted depth is predicted to 6 - 10 μm by FDM simulation at 22.5 kV.
- The brightness and the deformation of LPEB treated surface indicate the condition of 3 - 7 J/cm² and the 20 - 40 cycles is preferred. The corrosion resistance (R_{corr}) is improved by 45% at the '5 J/cm² - 40 cycles' with the 30% reduced COF.
- The microstructure of LPEB treated surface presents less grain boundary morphology with removed tool mark. The larger energy density and number of cycles cause the more defects such as crack, micro-pole, and $\beta\text{-Mg}_{17}\text{Al}_{12}$ particle aggregation due to inhomogeneous evaporation.
- According to EDS analysis, the '5 J/cm² - 40 cycles' is verified to fabricate maximum Al-enriched surface. The Al content of AZ31 is increased from 1.65 to 15.8 wt.% by LPEB process.
- Finally, the '5 J/cm² - 40 cycles' is selected to the optimum parameter of LPEB process for AZ31 and it shows similar EDS results at other Mg-alloys (AM60, AZ91).

5.2. Recommendations

Although the optimized LPEB process provides improved corrosion-protection performance, the limitations are remained such as relatively low corrosion characteristics and surface defects. For developing one-step surface treatment method of Mg-alloys, additional finishing mechanism and technology can be applied to in the LPEB system. The recommendations for future work are described.

[1] Hybrid LPEB nitriding process

In order to fabricate the denser microstructure on Mg-alloys, it can be applied to hybridize the LPEB process with PVD technologies. Among them, the nitriding is simply adapted into the LPEB system because its ion implantation apparatus could be set up in vacuum chamber of LPEB machine. High-frequency (10 MHz) & high-voltage (400 V) DC pulse power generator will be required to begin this study.

[2] Hybrid LPEB sintering process

Due to the inhomogeneous material composition of Mg-alloys, there are appeared many craters on LPEB treated surface. To reduce the unfavorable defects, it can be considered to applying hybrid LPEB process with powder sintering technology. The mechanism is scattering the Al powder on the working materials during LPEB process. Simultaneously, the powder could be filling at the inhomogeneous region and sintered by LPEB irradiation. This study will need the appropriate pump control technique with powder bead system in vacuum chamber.

[3] Vibrating table with electromagnetic coil system

It is proved that and electromagnetic field during LSM can activate distribution of grain structure at re-melted process [33]. Also, extreme high frequency vibration can affect the recrystallization of inhomogeneous Mg-alloys. For this reasons, the equipment is expected to deactivate the crater generation with well distributed surface layer. To enable vibrating motion in vacuum chamber, additional actuator will be designed. And it is considered that electromagnetic field can affect the electron beam direction.

REFERENCES

- [1] H. Friedrich and S. Schumann, "Research for a "new age of magnesium" in the automotive industry," *Journal of Materials Processing Technology*, vol. 117, pp. 276-281, 2001.
- [2] C. Castellani, R. A. Lindtner, P. Hausbrandt, E. Tschegg, S. E. Stanzl-Tschegg, G. Zanoni, *et al.*, "Bone-implant interface strength and osseointegration: Biodegradable magnesium alloy versus standard titanium control," *Acta biomaterialia*, vol. 7, pp. 432-440, 2011.
- [3] C. Berry. (2015). *A Closer Look at Magnesium*. Available: <http://www.discoveryinvesting.com/blog/2015/8/10/a-closer-look-at-magnesium>
- [4] marketsandmarkets.com (2015). *High Performance Alloys Market by Alloy Type (Wrought, Cast), by Product Type (Non-Ferrous Alloys, Refractory Alloys), by Alloying Element (Aluminum, Titanium, Magnesium), by Application (Aerospace, Industrial, Automotive), & Geography - Global Forecast to 2020*. Available: <http://www.marketsandmarkets.com/Market-Reports/high-performance-alloys-market-195251051.html>
- [5] S. Hao and M. Li, "Producing nano-grained and Al-enriched surface microstructure on AZ91 magnesium alloy by high current pulsed electron beam treatment," *Nuclear Instruments and Methods in Physics Research Section B: Beam Interactions with Materials and Atoms*, vol. 375, pp. 1-4, 2016.
- [6] M. Li, S. Hao, H. Wen, and R. Huang, "Surface composite nanostructures of AZ91 magnesium alloy induced by high current pulsed electron beam treatment," *Applied Surface Science*, vol. 303, pp. 350-353, 2014.
- [7] M. Li, S. Hao, and C. Dong, "Improved wear resistance of magnesium alloys AZ91 by high current pulsed electron beam treatment," *Transactions of the Indian Institute of Metals*, vol. 62, pp. 485-487, 2009.
- [8] B. Gao, S. Hao, J. Zou, W. Wu, G. Tu, and C. Dong, "Effect of high current pulsed electron beam treatment on surface microstructure and wear and corrosion resistance of an AZ91HP magnesium alloy," *Surface and Coatings Technology*, vol. 201, pp. 6297-6303, 2007.
- [9] S. Hao, B. Gao, A. Wu, J. Zou, Y. Qin, C. Dong, *et al.*, "Surface modification of steels and magnesium alloy by high current pulsed electron beam," *Nuclear Instruments and Methods in Physics Research Section B: Beam Interactions with Materials and Atoms*, vol. 240, pp. 646-652, 2005.
- [10] B. Gao, S. Hao, J. Zou, T. Grosdidier, L. Jiang, J. Zhou, *et al.*, "High current pulsed electron beam treatment of AZ31 Mg alloy," *Journal of Vacuum Science & Technology A: Vacuum*,

- Surfaces, and Films*, vol. 23, pp. 1548-1553, 2005.
- [11] Y. Uno, A. Okada, K. Uemura, P. Raharjo, S. Sano, Z. Yu, *et al.*, "A new polishing method of metal mold with large-area electron beam irradiation," *Journal of Materials processing technology*, vol. 187, pp. 77-80, 2007.
- [12] H. W. Park and I. Lee, "Large pulsed electron beam surface treatment of translucent PMMA," *Applied Surface Science*, vol. 308, pp. 311-315, 2014.
- [13] Y. Daichi, Z. Wang, K. Yamazaki, and S. Sano, "Investigation of the formation and energy density of high-current pulsed electron beams," *Plasma Chemistry and Plasma Processing*, vol. 27, pp. 458-472, 2007.
- [14] C. Chen, S. Splinter, T. Do, and N. McIntyre, "Measurement of oxide film growth on Mg and Al surfaces over extended periods using XPS," *Surface Science*, vol. 382, pp. L652-L657, 1997.
- [15] M. M. Avedesian and H. Baker, *ASM specialty handbook: magnesium and magnesium alloys* vol. 274: ASM international Materials Park, OH, 1999.
- [16] G. Song and A. Atrens, "Understanding magnesium corrosion—a framework for improved alloy performance," *Advanced engineering materials*, vol. 5, pp. 837-858, 2003.
- [17] Y. Yavor, S. Goroshin, J. M. Bergthorson, and D. L. Frost, "Comparative reactivity of industrial metal powders with water for hydrogen production," *international journal of hydrogen energy*, vol. 40, pp. 1026-1036, 2015.
- [18] N. Gupta, D. D. Luong, and K. Cho, "Magnesium matrix composite foams—density, mechanical properties, and applications," *Metals*, vol. 2, pp. 238-252, 2012.
- [19] J. Liao and M. Hotta, "Corrosion products of field-exposed Mg-Al series magnesium alloys," *Corrosion Science*, vol. 112, pp. 276-288, 2016.
- [20] Y. Ding, C. Wen, P. Hodgson, and Y. Li, "Effects of alloying elements on the corrosion behavior and biocompatibility of biodegradable magnesium alloys: a review," *Journal of materials chemistry B*, vol. 2, pp. 1912-1933, 2014.
- [21] M. O. Pekguleryuz, K. Kainer, and A. A. Kaya, *Fundamentals of magnesium alloy metallurgy*: Elsevier, 2013.
- [22] M. Golabczak, *Estimation of carbon coatings manufactured on magnesium alloys*: INTECH Open Access Publisher, 2011.
- [23] S. D. Ponja, I. P. Parkin, and C. J. Carmalt, "Magnesium Oxide Thin Films with Tunable Crystallographic Preferred Orientation via Aerosol-Assisted CVD," *Chemical Vapor Deposition*, vol. 21, pp. 145-149, 2015.
- [24] W. Tegart, "The electrolytic and chemical polishing of metals," *Chapter*, vol. 10, p. 96, 1959.

- [25] X. Dong, "Surface Treatments for Magnesium Alloys," in *Handbook of Manufacturing Engineering and Technology*, ed: Springer, 2015, pp. 3031-3054.
- [26] S.-j. Kwon, J.-y. Hur, C.-M. Lee, K.-s. Jang, S.-m. Moon, and H.-k. Lee, "A Study on How to Improve Magnesium Anodizing Process with High Biocompatibility," *한국표면공학회/지*, vol. 48, pp. 185-193, 2015.
- [27] R. Arrabal, E. Matykina, T. Hashimoto, P. Skeldon, and G. Thompson, "Characterization of AC PEO coatings on magnesium alloys," *Surface and Coatings Technology*, vol. 203, pp. 2207-2220, 2009.
- [28] B. Mingo, R. Arrabal, M. Mohedano, A. Pardo, and E. Matykina, "Corrosion and wear of PEO coated AZ91/SiC composites," *Surface and Coatings Technology*, 2016.
- [29] T. Tański, "Characteristics of Hard Coatings on AZ61 Magnesium Alloys," *Strojnicki Vestnik/Journal of Mechanical Engineering*, vol. 59, 2013.
- [30] T. Ishizaki, J. Hieda, N. Saito, N. Saito, and O. Takai, "Corrosion resistance and chemical stability of super-hydrophobic film deposited on magnesium alloy AZ31 by microwave plasma-enhanced chemical vapor deposition," *Electrochimica Acta*, vol. 55, pp. 7094-7101, 2010.
- [31] X. Peng, D. Edwards, and M. Barteau, "Formation of magnesium nitride layers on the Mg (0001) surface by ion implantation," *Surface Science*, vol. 185, pp. 227-248, 1987.
- [32] D. Höche, C. Blawert, M. Cavellier, D. Busardo, and T. Gloriant, "Magnesium nitride phase formation by means of ion beam implantation technique," *Applied Surface Science*, vol. 257, pp. 5626-5633, 2011.
- [33] J. Zhou, J. Xu, S. Huang, Z. Hu, X. Meng, and X. Feng, "Effect of laser surface melting with alternating magnetic field on wear and corrosion resistance of magnesium alloy," *Surface and Coatings Technology*, vol. 309, pp. 212-219, 2017.
- [34] J. D. Majumdar, R. Galun, B. Mordike, and I. Manna, "Effect of laser surface melting on corrosion and wear resistance of a commercial magnesium alloy," *Materials Science and Engineering: A*, vol. 361, pp. 119-129, 2003.
- [35] E. Rocca, C. Juers, and J. Steinmetz, "Corrosion behaviour of chemical conversion treatments on as-cast Mg–Al alloys: Electrochemical and non-electrochemical methods," *Corrosion Science*, vol. 52, pp. 2172-2178, 2010.
- [36] G. Bo, H. Yi, Z. Wenfeng, and T. Ganfeng, "Surface Modification of Mg Alloys AZ31 and ZK60-1Y by High Current Pulsed Electron Beam," in *Special Issues on Magnesium Alloys*, ed: InTech, 2011.

- [37] L. Zhao, Q. Liu, R. Gao, J. Wang, W. Yang, and L. Liu, "One-step method for the fabrication of superhydrophobic surface on magnesium alloy and its corrosion protection, antifouling performance," *Corrosion Science*, vol. 80, pp. 177-183, 2014.
- [38] C. Taltavull, B. Torres, A. López, P. Rodrigo, and J. Rams, "Novel laser surface treatments on AZ91 magnesium alloy," *Surface and Coatings Technology*, vol. 222, pp. 118-127, 2013.
- [39] J. Smolik, A. Mazurkiewicz, J. Kacprzyńska-Gołacka, M. Rydzewski, M. Szota, and J. Mizera, "Composite Layers "MgAl Intermetallic Layer/PVD Coating" Obtained On The AZ91D Magnesium Alloy By Different Hybrid Surface Treatment Methods," *Archives of Metallurgy and Materials*, vol. 60, pp. 1031-1035, 2015.
- [40] G. A. Mesyats, *Pulsed power*: Springer Science & Business Media, 2007.
- [41] S. I. Molokovsky and A. D. Sushkov, *Intense electron and ion beams*: Springer Science & Business Media, 2005.
- [42] L. E. Rehn, S. Picraux, and H. Wiedersich, *Surface alloying by ion, electron, and laser beams: papers presented at the 1985 ASM Materials Science Seminar, 12-13 October 1985, Toronto, Ontario, Canada*: Asm Intl, 1987.
- [43] D. Proskurovsky, V. Rotshtein, G. Ozur, A. Markov, D. Nazarov, V. Shulov, *et al.*, "Pulsed electron-beam technology for surface modification of metallic materials," *Journal of Vacuum Science & Technology A*, vol. 16, pp. 2480-2488, 1998.
- [44] V. Engelko, B. Yatsenko, G. Mueller, and H. Bluhm, "Pulsed electron beam facility (GESA) for surface treatment of materials," *Vacuum*, vol. 62, pp. 211-216, 2001.
- [45] Z. Zhang, J. Cai, L. Ji, X. Wang, Y. Li, S. Yang, *et al.*, "Microstructures and corrosion mechanism of AISI 304L stainless steel irradiated by high current pulsed electron beam," *Protection of Metals and Physical Chemistry of Surfaces*, vol. 50, pp. 650-658, 2014.
- [46] J. Kim, S. S. Park, and H. W. Park, "Corrosion inhibition and surface hardening of KP1 and KP4 mold steels using pulsed electron beam treatment," *Corrosion Science*, vol. 89, pp. 179-188, 2014.
- [47] V. Rotshtein and V. Shulov, "Surface Modification and Alloying of Aluminum and Titanium Alloys with Low-Energy, High-Current Electron Beams," *Journal of Metallurgy*, vol. 2011, 2011.
- [48] J. Walker, J. Murray, M. Nie, R. Cook, and A. Clare, "The effect of large-area pulsed electron beam melting on the corrosion and microstructure of a Ti6Al4V alloy," *Applied surface science*, vol. 311, pp. 534-540, 2014.
- [49] J. Kim and H. W. Park, "Influence of a large pulsed electron beam (LPEB) on the corrosion resistance of Ti– 6Al– 7Nb alloys," *Corrosion Science*, vol. 90, pp. 153-160, 2015.

- [50] J. Kim, W. J. Lee, and H. W. Park, "Mechanical properties and corrosion behavior of the nitriding surface layer of Ti 6Al 7Nb using large pulsed electron beam (LPEB)," *Journal of Alloys and Compounds*, vol. 679, pp. 138-148, 2016.
- [51] M. Jamshidinia, F. Kong, and R. Kovacevic, "Numerical modeling of heat distribution in the electron beam melting® of Ti-6Al-4V," *Journal of Manufacturing Science and Engineering*, vol. 135, p. 061010, 2013.
- [52] J. Goldak, M. Bibby, and A. Chakravarti, *A double ellipsoid finite element model for welding heat sources*: International Institute of Welding, 1985.
- [53] P.-F. Staub, "Bulk target backscattering coefficient and energy distribution of 0.5-100 keV electrons: an empirical and synthetic study," *Journal of Physics D: Applied Physics*, vol. 27, p. 1533, 1994.
- [54] S. Lee, H. J. Ham, S. Y. Kwon, S. W. Kim, and C. M. Suh, "Thermal conductivity of magnesium alloys in the temperature range from– 125 C to 400 C," *International Journal of Thermophysics*, pp. 1-8, 2013.
- [55] D. A. Porter, K. E. Easterling, and M. Sherif, *Phase Transformations in Metals and Alloys, (Revised Reprint)*: CRC press, 2009.
- [56] H. Liu, J. Liu, L. Ouyang, and C. Luo, "On the multiple orientation relationship of the Mg/ γ -Mg₁₇Al₁₂ precipitation system," *Journal of Applied Crystallography*, vol. 45, pp. 224-233, 2012.

ACKNOWLEDGEMENTS

I would never have been able to finish my thesis without the sincerely help, support, and guidance of professors, the senior and junior colleagues, friends and a lot of acquaintances.

Firstly, I would never forget excellent guidance of Prof. Hyung Wook Park as advisor of my graduate study of mechanical engineering in Ulsan National Institute of Science and Technology. His knowledge and insightful comments motivate and led me. Then, I am truly gratitude to Prof. Young-Bin Park and Prof. Namhun Kim. As thesis committee members, they readily provide me challenged inspirations for improvement of the manuscript.

Also, I am really appreciated to Multiscale-Hybrid-Manufacturing Laboratory members for truthful advice and counsel of Dr. Deka, Dr. Ankita, Dr. Nilanjan, Dr. Kyung-II Kong, Dr. Eunju Park, Dr. Dong Min Kim, Jisu Kim, Jaewoo Seo, Do Young Kim, Obum Kwon, Min Ji Kim, Young Bin Kim, and Yeon Oh Kim.

Especially, I would never finish my work without honest helps of Jisu Kim as senior researcher in electron beam manufacturing field. He truly helped me from basic education to correction of manuscript with helpful idea and thoughtful advice. Then, Dr. Dong Min Kim gave me new idea for preparation of the defense. Min Ji Kim and Young Bin Kim helped me from small to large in various sides during my stay at UNIST.

My work compromised of considerable assistances of MakeLab members; Gangwook Kwon, Jaehun Cha, Jinsik Kim, and Jung-II Young. I am really appreciated for the helps in the progress of specimen fabrication and surface profile measurement.

Finally, I want to give deepest gratitude to my parents for warm encouragement and incessant support to complete my master degree. My brother Woo Ram Lee also sincerely helped me throughout the all courses.

